Journal of Controlled Release 348 (2022) 849–869

Contents lists available at ScienceDirect

Journal of Controlled Release

journal homepage: www.elsevier.com/locate/jconrel

Hollow microneedle assisted intradermal delivery of hypericin lipid nanocapsules with light enabled photodynamic therapy against skin cancer

Heba Abd-El-Azim [a,b,c], Ismaiel A. Tekko [a,d], Ahlam Ali [e], Alyaa Ramadan [c], Noha Nafee [c], Nawal Khalafallah [c], Taifur Rahman [f], William Mcdaid [g], Rania G. Aly [h], Lalitkumar K. Vora [a], Steven J. Bell [f], Fiona Furlong [a], Helen O. McCarthy [a], Ryan F. Donnelly [a,*]

[a] School of Pharmacy, Queen's University Belfast, Medical Biology Centre, 97 Lisburn Road, Belfast BT9 7BL, UK
[b] Faculty of Pharmacy, Damanhour University, El Beheira, Egypt
[c] Faculty of Pharmacy, Alexandria University, Alexandria, Egypt
[d] Department of Pharmaceutics and Pharmaceutical Technology, Faculty of Pharmacy, Aleppo University, Aleppo, Syria
[e] Patrick G Johnston Centre for Cancer Research, Queen's University Belfast, Medical Biology Centre, 97 Lisburn Road, Belfast BT9 7BL, UK
[f] School of Chemistry and Chemical Engineering, Queen's University Belfast, UK
[g] Cancer Research UK Manchester Institute, Cancer Research UK Manchester Institute, The University of Manchester, Alderley Park SK10 4TG, UK
[h] Department of Pathology, Faculty of Medicine, Alexandria University, Alexandria, Egypt

ARTICLE INFO

Keywords:
Photodynamic therapy
Non-melanoma skin cancer, hypericin
Lipid nanocapsule, hollow microneedle

ABSTRACT

Photodynamic therapy (PDT) to manage non-melanoma skin cancers has garnered great attention over the past few years. Hypericin (Hy) is a potent lipid-soluble photosensitiser with promising anticancer therapeutic activities. Nevertheless, its poor water-solubility, aggregation in biological systems and insufficient skin penetration restricted its effective exploitation. Herein, we report for the first-time encapsulation of Hy into lipid nanocapsules (Hy-LNCs), and then application of an AdminPen™ hollow microneedles (Ho-MNs) array and an in-house fabricated Ho-MN to enable efficient intradermal delivery. The physicochemical properties, photoactivity, *ex vivo* drug distribution and cellular uptake were evaluated. Results showed that Hy-LNCs were successfully formed with a particle size of 47.76 ± 0.49 nm, PDI of 0.12 ± 0.02, high encapsulation efficiency (99.67% ± 0.35), 396 fold higher photoactivity, 7 fold higher skin drug deposition, significantly greater cellular uptake and higher photocytotoxicity compared to free Hy. The therapeutic effect of Hy-LNCs was finally assessed *in vivo* using a nude mouse model with transplanted tumours. Interestingly, Hy-LNCs delivered by Ho-MN exhibited remarkable anti-tumour destruction (85.84%) after irradiation with 595 nm. This study showed that Ho-MNs-driven delivery of Hy-LNCs followed by irradiation could form a promising minimally invasive, effective and site-specific approach for managing non-melanoma skin cancers.

1. Introduction

Skin cancer is the world's most common type of cancer. According to the World Health Organization (WHO), non-melanoma skin cancer has been increasing over the past decades, with a global estimation of over 1,000,000 cases reported annually, with a high mortality rate reaching one person dying every four minutes [1]. Currently used treatment strategies include surgical resection, chemotherapy, radiotherapy, immunotherapy and cryotherapy. However, these treatments have poor prognosis and underlie several systemic adverse effects [2]. Thus, it is urgent to exploit new efficient therapies for cancer.

Photodynamic therapy (PDT) is a promising alternative treatment modality for controlling malignant diseases as it offers several advantages over conventional strategies, including reduced long-term morbidity, low recurrence rates, applicability in combination therapy without compromising other treatment options, and very good cosmetic results [3]. PDT is a minimally invasive therapeutic approach that is based on local or systemic administration of a photosensitiser (PS) followed by light irradiation to generate reactive oxygen species (ROS) that selectively damage the diseased cells [4]. Ideally, PS should be harmless

* Corresponding author at: Pharmaceutical Technology, School of Pharmacy, Queen's University Belfast, Medical Biology Centre, 97 Lisburn Road, Belfast, BT9 7BL, Northern Ireland, United Kingdom.
E-mail address: r.donnelly@qub.ac.uk (R.F. Donnelly).

https://doi.org/10.1016/j.jconrel.2022.06.027
Received 21 January 2022; Received in revised form 22 April 2022; Accepted 15 June 2022
Available online 28 June 2022

to healthy and abnormal cells in the absence of light [5].

Local PDT has received increased attention in the preclinical research for non-melanoma skin cancer treatment as it has several advantages over systemic PDT. These include; a) minimized cumulative systemic toxicity, b) selective tumour destruction with minimal damage to normal cells, c) it could be used as a single or as adjuvant anticancer therapy [6], and d) the localised administration of PS would help in overcoming the necessity of avoiding light exposure that is usually required during and after treatment sessions of systemically administered PS which would improve the patient's compliance and quality of life [7]. Therefore, different targeted PDT strategies for localised effect were introduced in the literature, such as magnetic drug targeting using PS-loaded superparamagnetic nanoparticles [7] or the combination of PDT with electric field application [8]. However, these techniques underlie some difficulties, including the complexity of application and necessity of an external trigger, and the requirement of trained personnel. Thus, there was an urgent need to establish new targeted PDT approaches for efficient site-specific anticancer effects. This work presented an alternative strategy to address such a need.

Hypericin (Hy), a phenanthroperylenequinone derivative, is a naturally occurring photodynamic agent extracted from *Hypericum perforatum* (St John's wort). It is one of the most potent photosensitizing agents [9,10]. This photoactive compound is characterised by high efficiency in the production of singlet oxygen species and superoxide anions after irradiation and low or negligible dark toxicity [11]. Interestingly, Hy exhibited characteristic preferential accumulation in tumour cells and thus showed promising potential applications in photodynamic targeting of recurrent or unresectable malignancies, including skin, nasopharyngeal, bladder, pancreatic cancers and lymphomas [12,13]. Despite its potent tumouricidal activity, Hy forms insoluble lipophilic ion pairs at physiological pH due to its highly hydrophobic nature leading to low photoactivity and ineffective delivery to the cancerous cells [5]. Besides, the poor skin penetration adds another challenge hindering the Hy exploitation in PDT due to the fact that most of the topically applied Hy is accumulated in the *stratum corneum (SC)* tissue [14]. Consequently, finding new strategies to improve solubility, provide high photoactivity, boost successful intradermal delivery and provide sufficient protection of such delicate PS from the external environment has become very important.

Various nanocarriers have been used to incorporate Hy to overcome its low aqueous solubility and poor skin penetration, including using iron oxide [7,15], polymeric [16,17], and solid lipid nanoparticles [5,18]. Lipid nanocapsules (LNCs) encapsulating PSs for transdermal application have gained increasing attention due to their biocompatibility, enhanced permeability and better loading efficiency, as well as ease of preparation, scalability and cost-effective manufacturing LNCs are synthetic core-shell nanostructures with a lipid oil core and a surfactant shell giving them a unique hybrid structure between polymeric and lipid nanocarriers [19,20]. This unique structure enabled the LNCs to overcome the poor colloidal stability and to, significantly improve the low solubility of many drug molecules, and enhance transdermal/intradermal delivery of many anticancer and photosensitive compounds. Moreover, LNCs showed a great potential to encapsulate Hy, itself. Barras and colleagues [21] incorporated Hy into LNC alone or in combination with protoporphyrin [22]. Their Hy-loaded LNCs enhanced the *in vitro* photoactivity and slowed the growth of xenograft tumours in mice. However, due to inefficient transdermal/intradermal delivery, the impact of colloidal carriers on improving the dermal penetration of Hy was limited and mainly confined to the superficial skin layers [23,24].

Microneedles (MNs) are minimally invasive micron-sized devices designed to painlessly penetrate *SC* barrier for more efficient transdermal/intradermal drug delivery [25,26]. MNs have been used successfully to deliver a wide range of drug molecules, including higher molecular weight biologics and vaccines, hydrophilic and hydrophobic drugs [27–29]. Different types of MNs were fabricated, including solid (poke and patch), coated (coat and poke), dissolving (poke and release), hydrogel-forming (poke and swell) and hollow ones (poke and flow).

Hollow microneedles (Ho-MNs) are designed with microfluidic channels that disrupt the upper layers of the skin upon application creating micro-conduits to deliver liquid medications or extract biological fluids. Ho-MNs have been used for intradermal and subcutaneous deposition of versatile nano- and microparticulate formulations [30,31]. In addition, Ho-MNs have been translated to commercially available products such as MicronJet™, DebioJect™, Soluvia™, Intanza™, MicroTrans™ h-Patch™, and AdminPen™ Ho-MNs liquid injection devices (600, 900, 1200, and 1500 μm), that can be mounted on any available standard syringe [30].

Herein, we systematically study the feasibility of the microneedle-assisted nanoparticle delivery concept for localised PDT. First, Hy was encapsulated into lipid nanocapsules (LNCs), to prevent its aggregation and enhance its uptake by cancerous cells and then delivered into the tumour using in-house fabricated Ho-MN as a minimally invasive, user-friendly, effective intradermal delivery system to overcome its poor transdermal penetration. Secondly, we have combined Ho-MN based Hy-LNC with light for enhanced, localised, effective PDT and antitumour activity of Hy as a potentially effective approach to treat non-melanoma skin cancers.

2. Materials and methods

2.1. Materials

Hypericin was purchased from Planta Natural Products GmbH, Austria. Labrafac® WL 1349 (caprylic-capric acid triglycerides) was provided by Gattefossé S.A., Saint-Priest, France. Solutol® HS 15, Kolliphor® HS 15, Macrogol (15) - hydroxystearate, Polyethylene glycol (15) hydroxystearate, Polyoxyethylated 12 – hydroxystearic acid (a mixture of free polyethylene glycol 660 and polyethylene glycol 660 hydroxystearate) were obtained from Sigma Aldrich, Dorset, UK. Lipoid® S 100 (a soybean lecithin at 97% of phosphatidylcholine) was a kind gift from Lipoïd GMBH Ludwigshafen, Germany. Poly lactic acid (PLA 3D850) biopolymer was purchased from Nature Works LCC, Minnetonka, MN, USA. Dimethyl sulfoxide, DMSO, >99.5%, was obtained from Honeywell Specialty Chemicals Seelze GmbH, Wunstorfer Strabe, Seelze, Germany. Light-emitting diode (LED) with 595 ± 10 nm, 445 mW and 700 mA mounted with adjustable collimation optic was purchased from Thorlabs GmbH, Germany. AdminPen™ device was purchased from NanoBioSciences LLC, USA. Matrigel® was obtained from Corning, UK. Isoflurane inhaled anaesthetic agent was purchased from AbbVie Ltd., Maidenhead, UK. Only ultra-pure water (Milli-Q Millipore, USA) was used. All other chemical reagents were commercially obtained as reagent-grade products.

2.2. Preparation of Hypericin-loaded lipid nanocapsules (Hy-LNCs)

Hy-loaded LNCs and drug-free (which is used as a control to study the effect of adding the drug on LNCs properties) were prepared by phase inversion method as previously described [20,44,45] with minor modifications. To prepare a drug-free LNCs, briefly, Labrafac® (5% *w*/w), Kolliphor ® HS 15 (5% w/w), Lipoid® S 100 (0.75% w/w), NaCl (0.44% w/w) and water were mixed using magnetic stirring at room temperature and then heated progressively to 85 °C. After that, it cooled down to 65 °C. Five temperature cycles were applied to obtain the required LNC with the desired properties. During the last cooling phase in the fifth cycle at 78 °C (the phase inversion temperature), the system was irreversibly shocked by adding cold (2 °C) deionized water that equates 3 times of formula volume which led to forming of stable LNCs. Then, the formulation was further stirred for 10 min. The prepared LNCs were stored in the fridge at a temperature of 2–8 °C until further use.

Hy-loaded LNCs (Fig. 1(I)), a Hy solution in DMSO (0.5 mg/ml) was first prepared then the required volumes were quickly injected into the LNCs formulation during the heating phase of the third cycle. Followed

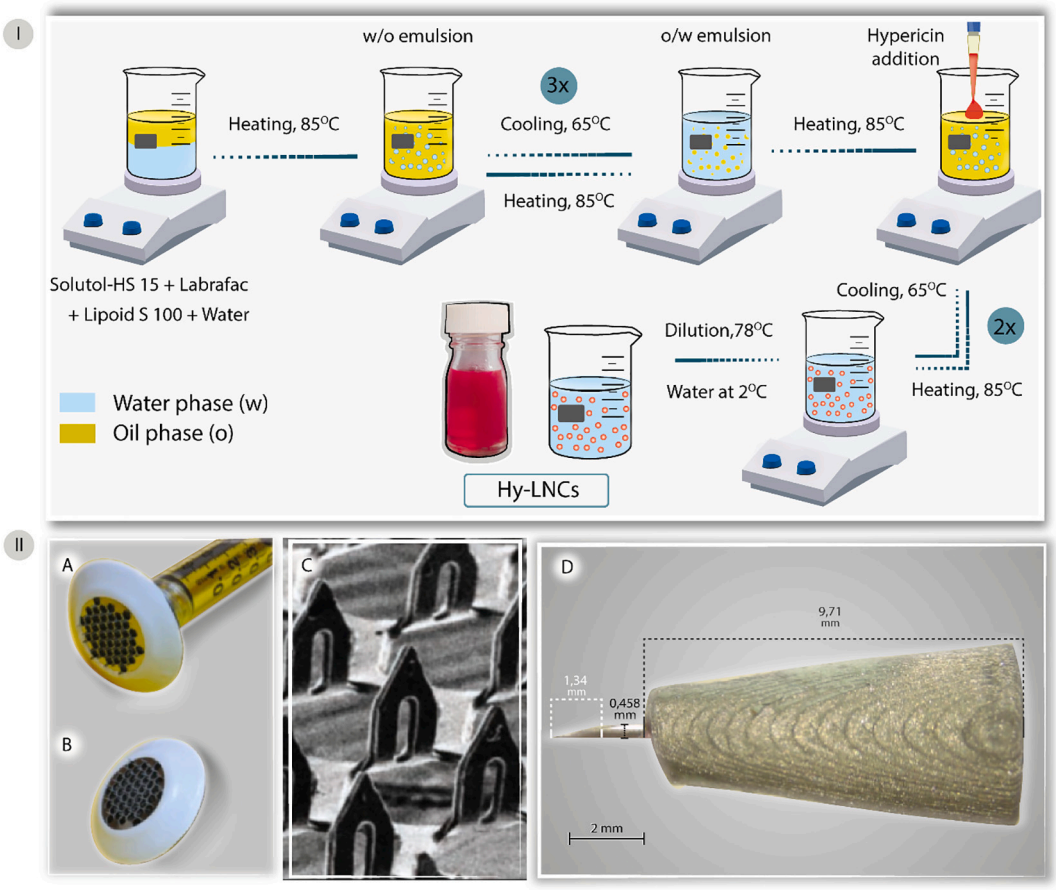

Fig. 1. I) Schematic representation for the preparation of Hy-LNCs by modified phase inversion method. **II)** AdminPen™ device; **A, B)** Showing 43 metallic hollow stainless-steel microneedles of 1200 μm in length and 1 cm^2 of circular microneedle array, and **C)** SEM image (Image was used with permission from AdminMed) [1] **D)** Assembled single hollow microneedle with 1300 μm bevelled shaft.

by two more temperature cycles and continued as described above. This resulted in forming Hy-loaded LNCs with total drug concentrations of 10, 100, and 200 μM, respectively. The Hy-LNCs were stored in the fridge at a temperature of 2–8 °C until further use.

2.3. Characterization of hypericin-loaded lipid nanocapsules

2.3.1. Particle size and zeta potential measurement

LNCs particle size, polydispersity index (PDI) and zeta potential were measured by dynamic light scattering using a NanoBrook Omni particle sizer and zeta potential analyser (Brookhaven Ins., USA) equipped with a 90° scattering angle. The measurements were performed at 25 °C after 100-fold sample dilution was done using ultrapure water (Milli-Q, Millipore, USA). For zeta potential measurement, electrophoretic mobilities were converted to potentials using Smoluchowski's equation as previously described [32,33].

2.3.2. Transmission Electron microscope studies

The shape of the NCs was evaluated using transmission electron microscopy (TEM). Samples were deposited on carbon-coated copper grids with 200 meshes (PELCO®, TED PELLA INC., USA), diluted in ultrapure water (1:10 *v*/v), stained with phosphotungstic acid and dried for 24 h at room temperature. The microscope (Joel JEM 1400 Plus TEM, USA) was operated with an accelerating voltage of 100 kV [34,35]. For morphological analysis, the TEM was operated in bright field mode with a magnification >10,000×.

2.3.3. Drug content and encapsulation efficiency determination

Loaded LNCs were assessed for Hy content and entrapment efficiency by measuring the total drug amount and the free drug concentration in the aqueous phase, respectively. For Hy content, the total drug amount was determined after solubilizing the LNCs in tetrahydrofuran/methanol mixture, using HPLC analysis at 590 nm. The drug content (DC%) was calculated according to the following equation:

$$DC\% = \left(\frac{\text{Total drug amount}}{\text{Initial drug amount added}}\right) \times 100 \quad (1)$$

Entrapment efficiency (EE%) of Hy-LNCs was evaluated by separating the drug-loaded LNCs from the free drug using ultracentrifugation (Sigma 2-16KL Refrigerated Centrifuge, Sigma Lab GmbH, Germany) through Amicon® ultracentrifugal filters (100 K MWCO) at 14000 rpm and 4 °C for 30 min. The encapsulated drug was determined after solubilizing the LNCs in tetrahydrofuran/methanol mixture, using HPLC analysis at 590 nm, as described in Section 2.5. The EE% was estimated according to the following equation:

$$EE\% = \left(\frac{\text{Encapsulated drug amount}}{\text{Initial drug amount added}}\right) \times 100 \quad (2)$$

2.3.4. Photodynamic activity measurement

The photodynamic efficiency of Hy-LNCs in relation to Hy solution was assessed by determining the rate constant for the photodecomposition of uric acid (UA) as a singlet oxygen scavenger and a chemical dosimeter [36]. Various solutions were prepared from Hy solution (as a control) or Hy-LNCs that have drug concentrations of 10, 100 and 200 μM with added UA and tween 20 at concentrations of 1.8×10^{-4} mol L^{-1}

0.001% in PBS (pH 7.0), respectively. The Aliquots of each of these solutions were irradiated with a LED at 595 ± 10 nm and 27.38 ± 3.45 mW cm^{-2} = 273.84 ± 34.59 W m^{-2} for 0, 5, 10, 15, 20, 25 and 30 min. The absorbance of the solution was recorded spectrophotometrically at 292 nm using FLUO star® Omega spectrophotometer (BMG labtech, Germany), and the photodecomposition constant of UA was determined. Baseline correction was performed using blank LNCs in PBS and 0.001% Tween 20 to nullify and possible interfering absorption arising from the LNCs components [18]. The photodynamic activity (PA) was calculated based on the following equation:

$$PA = \frac{\Delta A_{UA}.10^5}{E_0.t.A_{PS}(\lambda_{irr})} \quad (3)$$

with PA = photodynamic activity [m^2 W^{-1} s^{-1} = m^2/J]; ΔA_{UA} = UA absorbance decrease at 292 nm in UA-PS solution after irradiation; E_0 fluence rate [W m^{-2}]; t = irradiation time [s]; A_{PS} (λ_{irr}) = absorbance of PS in UA-PS-solution at irradiation wavelength.

2.3.5. Photostability determination

The photostability of encapsulated Hy compared to Hy in DMSO solution was evaluated as previously described with minor modifications [18]. The photodegradation of Hy was monitored by recording the change in peak area using the developed and validated HPLC method with UV detector operated at 590 nm as described in pharmaceutical analysis section. Briefly, 3 ml of Hy DMSO solution or Hy-LNCs (100 μM) was exposed to light delivered by a LED at 595 ± 10 nm and 27.38 ± 3.45 mW cm^{-2} for 0, 10, 20, 30 and 40 min. For the Hy-LNCs, the drug was extracted after solubilizing the LNCs in tetrahydrofuran/methanol mixture and centrifugation at 12,000 rpm for 15 min to precipitate any residual lipids. A sample was then withdrawn from the supernatant and analysed using the validated HPLC method. The amount of Hy, in μg, in each sample was calculated.

2.3.6. Evaluation of Hypericin cellular uptake and photocytotoxicity

In this study, the B16-F10 (CRL-6475™), a mouse melanoma cell line obtained from the American Type Culture Collection (ATCC) was used. The cells were grown as adherent monolayers in Dulbecco's Modified Eagle Medium (DMEM, Thermo Fisher Scientific, UK) supplemented with 10% Fetal Bovine Serum (FBS) and 1% Penstrep (10,000 U.I. ml^{-1} penicillin and 10 mg/ml streptomycin and maintained at 37 °C in a humidified 5% CO_2 incubator [2]. Sub-confluent monolayers of the cells were washed with sterile PBS and then were detached with 5× trypsin diluted from Gibco® 0.5% Trypsin-EDTA (10×) (Thermo Fisher Scientific, UK) and living cell count was performed with a haemocytometer (Countess® II FL Automated Cell Counter, Life Technologies™ Corporation, USA) using the trypan blue exclusion method using (Tryptan Blue solution, 0.4%, VWR Life Science, UK) [37].

Cellular uptake of Hy into melanoma cell lines was evaluated by confocal imaging as well as flow cytometry. For confocal microscopy, samples consisting of a 10 ml suspension containing 1.41 × 10^6 cells ml^{-1} of B16-F10 were seeded in multi-chamber slides (Ibidi GmbH, Germany). After 24 h, the culture media were removed and replaced with the same amount of fresh media containing equalized concentrations of Hy (0 to 1 μM) in LNCs. After 2 h incubation, the media were removed, the cells were washed with PBS and fixed with 4% formaldehyde. Fluoromount DAPI mounting medium (Sigma Aldrich, Dorset, UK), for nuclei visualization, was added prior to imaging using Leica TCSP8 Confocal Laser Scanning Microscope (Leica Microsystems GmbH, UK) connected to an inverted DMi8 microscope. *Z*-stacks of the confocal images were rendered into 3D mode using LAS X software.

For quantitative evaluation of cellular uptake, samples of B16-F10 treated with Hy or Hy-LNCs were flow cytometrically assessed using BD Accuri C6 Plus Flow Cytometer (BD Life Sciences Biosciences, USA) [49]. Briefly, after 48 h incubation in a 96-well plate, melanoma cells were treated with different concentrations (0.1 to 3 μM) of free Hy or Hy-LNCs. Half of the treated plates were irradiated with 595 ± 10 nm LED (Thorlabs GmbH, Germany) with a light dose of 50 Jcm^{-2} and fluence rate of 27.38 ± 3.45 mW cm^{-2}, while the other half was kept in the dark. After 2 h, the cells were washed with PBS, Trypsinized and centrifuged at 20000 rpm for 10 min. Then, the cell pellets were resuspended in PBS and assessed for the fluorescence intensity% using flow cytometry.

To evaluate Hy photocytotoxicity, a preliminary study on the dark toxicity of free Hy and Hy-LNCs at different concentrations (0.1 to 5 μM) for B16-F10 was done. Afterward, the phototoxic effects of free Hy and Hy-LNCs at various concentrations were further examined. In these experiments, 2.12 × 10^6 cells ml^{-1} suspended in DMEM supplemented with 10% FBS and 1% Penstrep were plated in 96-well plates and grown at 37 °C and 5% CO_2 for 2 h. Then, the cells were irradiated with 595 ± 10 nm LED (Thorlabs GmbH, Germany) with a light dose of 50 Jcm^{-2} and fluence rate of 27.38 ± 3.45 mW cm^{-2}. After irradiation, the cells were re-incubated for an additional 24 h to evaluate cell survival using the MTS tetrazolium assay method [50]. This live cell counting method is based on the reduction of the Cell Titer 96® Aqueous One Solution Cell Proliferation Assay reagent (3-(4,5-dimethylthiazol-2-yl)-5-(3-carboxymethoxyphenyl)-2-(4-sulfophenyl)-2H-tetrazolium, Promega, UK) to a majority of water soluble purple formazan by the active mitochondrial dehydrogenases [51]. After the 24 h incubation period, the used DMEM was removed and the cells were treated with the MTS reagent at 0.19 mg/ml in DMEM for 1 h. Then, the absorbance at 490 nm was measured in a microplate reader (FLUO star® Omega, BMG labtech, Germany). The cell viability % was plotted as a function of the Hy concentration.

2.3.7. Stability evaluation

The effect of storage time on the different LNCs was monitored for up to 7 months. Formulations were stored in dark conditions at 2–4 °C and evaluated in relation to particle size, polydispersity index, zeta potential, drug content and EE. Samples were withdrawn, in triplicates, at predetermined time points (0, 3, 7, 14, 30, 90, 150, 210 days).

2.4. Evaluation of hollow microneedles-assisted delivery of Hypericin-loaded lipid nanocapsules

Hy-LNCs was delivered into the skin by either a commercially available stainless-steel Ho-MNs array, namely AdminPen™ Ho-MNs that consists of baseplate bearing of 43 MNs, each MN measures 1200 μm in height (Fig. 1 (II) A,B and C) or in-house fabricated stainless-steel single hollow MN (S-Ho-MN) that measures 1300 μL in height (Fig. 1(II) D).

2.4.1. Fabrication of single hollow microneedle

A single hollow microneedle (S-Ho-MN) measuring 1300 μm in height (Fig. 1(II) D) was fabricated in-house using a 26G × ½ inch stainless steel Terumo® needle (Terumo Europe, Leuven, Belgium). To obtain the required length, a conical-shaped PLA base (9.7 × 5 mm) was 3D-printed using an Ultimaker 3 (Ultimaker B.V., Geldermalsen, The Netherlands) FFF system and Cura® software. The printed base and 26G × ½ inch stainless steel Terumo® needle were then assembled to create a S-Ho-MN with the required height. The assembled S-Ho-MN was attached to a pre-filled syringe and used to deliver Hy formulations into the skin.

2.4.2. Evaluation of hollow microneedles properties

2.4.2.1. Insertion properties assessment. The *in vitro* insertion property of AdminPen™ Ho-MNs and S-Ho-MN, was evaluated using Parafilm M® (Bemis Company Inc., Soignies, Belgium), a validated synthetic skin-simulant membrane as previously described [38]. Briefly, a stack of ten layers of Parafilm M® (≈ 1.25 mm thickness) was placed on dental

wax support. Then, the AdminPen™ Ho-MNs was carefully pressed into the folded Parafilm M® layer using both the thumb and index finger by gently applying enough force to ensure complete contact between the entire front device surface and the membrane layers.

After 30 s of pressed insertion, the Ho-MNs were removed, the Parafilm M® layers were then separated, the number of visible holes created by Ho-MNs in each layer was counted, and the percentage of penetration was calculated according to the following Eq. [39]:

$$The\%of\ penetration = \frac{Number\ of\ created\ holes}{Actual\ number\ of\ hollow\ microneedles} \times 100 \quad (4)$$

MNs insertion into full-thickness excised neonatal porcine skin was also evaluated by both digital microscopy using a Keyence VHX- 700F Digital Microscope (Keyence, Osaka, Japan) and Optical Coherence Tomography (OCT) imaging using an EX1301 OCT microscope (Michelson Diagnostics Ltd., Kent, UK) immediately after insertion [40].

Prior to this study, excised skin samples were obtained from stillborn piglets <24 h after birth and stored at −20 °C in Petri dishes until further use. Prior to the experiments, the skin samples were shaved using disposable razors and were equilibrated in phosphate buffered saline (PBS), pH 7.4, for 20 min. The upper surface of the skin was cleaned and dried with tissue paper, and the skin was placed, dermis side down, on a 500-μm-thick sheet of dental wax. The AdminPen™ MNs were inserted into the skin using both the thumb and the index finger and pressed for 30 s.

After the removal of Ho-MNs, the skin was viewed under a digital microscope. The number of visible holes created by Ho-MNs was counted and the percentage of percutaneous penetration was also calculated according to Eq. (1). The skin was examined under OCT, and the depth of skin penetration was calculated.

In order to assess the penetration capability of the assembled S-Ho-MN, the MN was inserted into eleven layers of Parafilm M® (≈ 1.4 mm thickness) as a skin simulant membrane for MN insertion studies, following the same protocol as outlined above. Then, OCT images were recorded using an EX1301 OCT Microscope (Michelson Diagnostics Ltd., Kent, UK). The insertion depth of S-Ho-MN was estimated by measuring the height of inserted needle using the imaging software, ImageJ® (National Institute of Health, Bethesda, MD, USA).

2.4.3. Pore closure kinetics

The time required for full pore closure and skin recovery was observed by recording OCT images using an EX1301 OCT Microscope at 0, 2, 4, 6, 8, and 10 min after insertion of AdminPen™.

2.4.4. Ex vivo dermatokinetic studies

Ex vivo drug delivery efficiency and drug distribution in various skin layers from Hy-LNCs and Hy-DMSO solution, as a control, was evaluated using two techniques: quantitatively *via* cryostat sectioning and qualitatively using confocal microscopy. Quantitative analysis of Hy in excised porcine skin was performed, as previously reported [41], with minor modifications. Both Hy solution and Hy-LNCs were injected into full-thickness excised neonatal pig skin using AdminPen™ Ho-MNs. The upper surface of the skin was cleaned, dried with tissue paper, and the skin was placed, dermis side down, on a 500-μm-thick sheet of dental wax. The AdminPen™ Ho-MNs fitted with a formulation-prefilled syringe was inserted into the skin using both the thumb and the index finger by applying a force equivalent to that used to press a stamp onto an envelope for 30 s. Following insertion, the formulation was slowly injected into the skin. Then, Ho-MNs were slowly removed out from the skin.

After 1 h, the MN-treated skin region was excised using a biopsy bunch (12 mm diameter) (Stiefel, Middlesex, UK) and embedded in optimal cutting temperature embedding medium (Tissue-Tek, Sakura Finetek, CA, USA). The skin sample was snap-frozen in liquid nitrogen and sliced into 50 μm-thick sections using a Leica CM1900 Cryostat Microtome (Leica Microsystems, Nussloch, Germany), and five consecutive slices were collected into 0.5 ml microtubes. This procedure was continued until the whole biopsied skin was sliced. To analyse the amount of Hy distributed and deposited into each 5 slices, 300 μL of acetonitrile was added to the tissue sections. Each microtube was vortexed for 30 min to extract the drug and the sample was then centrifuged at 12,000 rpm for 15 min to precipitate any skin and media residuals. A sample was then withdrawn from the supernatant and analysed using HPLC method as described in Section 2.5. The amount of distributed Hy, in μg, was plotted against the average skin depth in μm. The total cumulative amount of deposited Hy was also calculated.

Additionally, dermal distribution of Hy from DMSO solution and LNCs was then further elucidated using confocal microscopy using Leica TCSP8 Confocal Laser Scanning Microscope (Leica Microsystems GmbH, UK) connected to an inverted DMi8 microscope. *Z*-stacks of the confocal images were rendered into 3D mode using LAS X software. A z-stack could be defined as a sequence of basic images captured at the same horizontal position (x, y) but at various imaging depths (z) [42]. In brief, the formulations were injected into the skin using the Ho-MNs array. Then, after 1 h, the biopsied skin samples were cryo-sectioned as described above. Each 50 μm-slice was placed on a glass slide and transverse as well as longitudinal section images were taken.

Ex vivo skin deposition of Hy in DMSO solution form, LNCs was performed in the excised porcine skin as reported previously after suitable modification [43]. The upper surface of the skin was cleaned, cut into 1 cm^2 pieces, and dried with tissue paper, and the skin was placed, dermis side down, on a 500-μm-thick sheet of dental wax. The formulations were slowly injected using the S-Ho-MN. At predetermined time points (0.5, 2, 4 and 6 h), each skin sample was washed with deionized water to remove any excess formulation and placed in 2 ml microtube. To extract the Hy, each tube was then heated in a water bath at 60 °C for 2–3 min and 1.5 ml of acetonitrile. The samples were homogenized utilizing Tissue Lyser LT (Qiagen, Ltd., Manchester, UK) at 50 Hz for 15 min and then centrifuged at 12,000 rpm for 15 min to precipitate any skin residuals. A sample was then withdrawn from the supernatant and analysed using HPLC method according to the same protocol mentioned in Section 2.5. The percentage recovery of Hy was plotted against time. The total cumulative amount of deposited Hy was also calculated.

A Leica SP8-MP Multiphoton Excited Fluorescence Microscope (Leica Microsystems GmbH, UK) equipped with a DM6000CFS fixed stage Upright Microscope was used to record the distribution of Hy from DMSO solution and LNCs in full-thickness porcine skin [44]. *Z*-stacks of the multiphoton images were rendered into 3D mode using LAS X software. The formulations were injected into the skin using the S-Ho-MN and the images were taken 2 h after treatment.

2.5. Pharmaceutical analysis

Quantification of Hy was performed using the reversed-phase high-performance liquid chromatography (HPLC) method that was developed by modifying a published assay [45].

Chromatographic separation was achieved using Agilent 1220® Infinity LC system (Agilent Technologies UK Ltd., Stockport, UK) with a XBridge™ BEH300 C18 5 μm column (150 × 4.6 mm; Waters Corporation, Milford, USA) with isocratic elution and UV detection at 590 nm. The mobile phase was a mixture of methanol: 18.37 mM potassium dihydrogen phosphate buffer (pH 3.5 adjusted using orthophosphohoric acid) (95:5 *v*/v) with a run time of 10 min per sample and flow rate of 1.4 ml/min. The column temperature was 30 °C and the injection volume was 30 μL. The chromatograms obtained were analysed using Agilent ChemStation® Software B.02.01. The HPLC method was validated according to the guidelines of the International Conference on Harmonisation (ICH,2005).

2.6. In vivo study

The delivery efficiency of our microneedles, drug distribution and its

therapeutic effects were evaluated *in vivo* using a nude mouse model with transplanted tumours. The *in vivo* studies were approved by the Committee of the Biological Services Unit, Queen's University Belfast. The work was carried out under Project License PPL 2794 and Personal Licenses PIL 1747 and 1732. All experiments were conducted in accordance with the policy of the Federation of European Laboratory Animal Science Associations and the European Convention for the protection of Vertebrate Animals used for experimental and other scientific purposes, implementing of the principles of the 3Rs (replacement, reduction and refinement).

In vivo experiments were performed on 20 female Balb/C nude mice aging 8–10 weeks and weighing 19.80 ± 0.90 g as an animal model. Mice were acclimatized to the laboratory conditions for a minimum of 1 week prior to the commencement of the experiments.

2.6.1. Mouse tumour model

The CT-26 (CRL-2638™), a mouse colon cell line obtained from the ATCC was used to establish the animal tumour model. The cells were cultured in RPMI 1640 (Thermo Fisher Scientific, UK) containing 10% FBS and 1% Penstrep. After being confluent, 5×10^6 CT-26 cells were implanted subcutaneously onto the flanks of the mice using Matrigel (Corning, UK).

2.6.2. Study design and experimental procedures

The animals were divided into four cohorts. The first cohort ($n = 4$) served as the untreated positive control, the second cohort (n = 4) was treated with LED light only, the third cohort ($n = 5$) was treated with Hy-LNCs only, and the fourth cohort ($n = 7$) was treated with both Hy-LNCs and LED light. The mice in each cohort were kept in a separate cage to avoid any interference that might affect the results. Treatment was initiated when the average volume of the tumour reached 100 mm^3. The assembled S-Ho-MN was used to deliver a daily dose of 1 mg/kg of the Hy-LNCs (equivalent to 25 μg of Hy) into the tumour mass. Mice received four doses throughout the study. Irradiation the tumour-bearing region only was done 45 min after drug administration, using the same 595 ± 10 nm LED (Thorlabs GmbH, Germany) that was used in the *in vitro* studies with a light dose of 230 Jcm^{-2} and fluence rate of 45 ± 2 mW cm^{-2}. During drug administration and irradiation, mice were anesthetized through a facial mask by isoflurane 5% *v*/v, 2 L/min. Mice were observed until recovery was achieved. Any animal with 20% weight loss during the study was to be removed for euthanasia, but this did not occur.

2.6.3. Evaluation of Hypericin distribution in the tumour tissue and the other body organs

To evaluate drug distribution in the tumour tissue and its potential transport to the rest of the body organs. After 45 min of the Hy-LNCs application using the S-Ho-MN and before the commencement of irradiation, mice were subjected to 2D imaging using Bruker image station system (Xtreme, Bruker, Billerica, USA). During imaging, Hy fluorescence intensity was recorded to evaluate drug biodistribution. Hy was excited at 480 nm and the fluorescence intensity was recorded at 600 nm [46]. Both treated and untreated animals were imaged at the same time point. To facilitate imaging, animals were placed in a chamber and sedated using isoflurane 5% *v*/v, 2 L/min. At the end of the experiment, mice were observed until they recovered.

2.6.4. Evaluation of Hypericin antitumour activity

To evaluate the anti-tumour activity of our Hy-LNCs formulation, the change in tumour size was monitored daily. The tumour dimensions were measured using an Electronic digital caliper (150 mm 8 Inch Carbon fiber Composites Digital Caliper). The tumour volume was subsequently estimated according to the formula [46]:

$$Tumor\ Volume\ \left(mm^3\right) = \frac{Width^2 \times Length}{2} \quad (5)$$

2.6.5. Histology study

For histological examination, mice were humanely culled by carbon dioxide rising concentrations in day 5 of the experiments. Tumour dissection was done immediately after death. The excised skin biopsies from all groups were fixed in 10% buffered formalin and processed in xylene and different grades of alcohol, then embedded in paraffin blocks and sectioned into 5 mm tissue section thickness. The sections were stained with haematoxylin–eosin (H&E) and examined under a light microscope (Leica, Germany) with different magnification to assess the viable tumour, and treatment effect in the form of necrosis, inflammation and fibrosis.

2.7. Statistical analysis

All the results were expressed as the mean ± SD ($n = 3$ for the *in vitro* and $n = 4$ for the *in vivo*, at least), and the significance was assessed using student's *t*-test and one-way ANOVA using the Prism software. Tukey *post hoc* test was established. One-way ANOVA was used to determine the significance of changes in LNCs stability study, photodynamic activity, cellular internalization, cell viability and tumour size in mice. Student's t-test was used to evaluate the significance of changes in drug photostability assessment and *ex vivo* skin deposition of Hy after MN application. *P*-Values <0.05 were considered significant.

3. Results and discussion

3.1. Development and characterization of Hypericin-loaded lipid nanocapsules

The criteria were set to prepare Hy-LNCs with homogenous particle size, < 100 nm, and high entrapment efficiency so that they can prevent drug aggregation in the skin after administration and can diffuse readily into the tumour cells after MNs application allowing for improved cellular uptake, enhanced photoactivity and cytotoxicity.

Hy-LNCs were formulated using small amounts of DMSO, a class 3 solvent according to the ICH harmonised guidance for residual solvents Q3C, R6. Hy-LNCs (with lipid concentration of 112 mg/ml) were successfully produced by the phase inversion process. The prepared LNCs possess a shell of PEG in their outer part and Lipoid® in their inner part, protecting an oily liquid core of Labrafac®. The hydrophilic/lipophilic nature of Kolliphor® enabled the phase inversion from o/w to w/o emulsion, and *vice versa*, by increasing the temperature and allowed the formation of stable smaller particles [47]. Lipoid® contributes to the formation of stable and well-structured LNCs [48]. In addition, the salinity exerted by NaCl increased the conductivity, thus helping to lower phase inversion temperature [47]. Importantly, Hy stability was confirmed throughout the heat cycles required to produce drug-loaded LNCs, with >99% of the drug remaining intact (data is not reported here).

Hy was loaded into LNCs in three different concentration levels; low (10 μM, Hy-LNCs 1), intermediate (100 μM, Hy-LNCs 2) and high (200 μM, Hy-LNCs 3). The formulations were screened for colloidal properties, encapsulation efficiency and photodynamic activity. The optimum formulation was then selected for further *in vitro* photocytotoxicity, cellular internalization, microneedles application, and *in vivo* study.

3.1.1. Particle size and zeta potential measurement

Particle size increased significantly (One-way ANOVA, $P < 0.0001$) from 37.77 ± 0.41 nm (PDI = 0.04 ± 0.01) to 76.88 ± 5.95 nm (PDI = 0.19 ± 0.01) by increasing the drug loading from 10 to 200 μM as shown in Table 1. However, for all formulations, the PDI was <0.2 (ranged between 0.07 ± 0.05 to 0.19 ± 0.01), indicating homogenous particle size distribution and monodisperse LNCs. Incorporating high amounts of Hy concentration to 200 μM into LNCs resulted in a significant increase in the particle size of LNCs, while no effect on size was observed in the

Table 1
Physicochemical properties, encapsulation efficiency and drug content of blank and Hy-LNCs. Data reported as mean ± SD, $n = 3$.

Parameter	B-LNCs	Hy-LNCs 1	Hy-LNCs 2	Hy-LNCs 3
Drug concentration (μM)	0	10	100	200
Particle size (nm)	37.61 ± 1.64	37.77 ± 0.41	47.76 ± 0.49	76.88 ± 5.95
PDI	0.07 ± 0.05	0.04 ± 0.01	0.12 ± 0.02	0.19 ± 0.01
Zeta potential (mV)	−1.74 ± 0.26	−2.08 ± 0.89	−4.31 ± 1.93	−12.25 ± 2.43
EE%	–	100 ± 0.03	99.67 ± 0.35	89.64 ± 0.44
DC%	–	98.16 ± 2.47	100.00 ± 3.72	100.00 ± 1.63

case of low drug concentration (10 μM).

The prepared LNCs showed slightly negative zeta potential (−1.74 ± 0.26 for blank LNCs, B-LNCs) that is likely ascribed to the presence of PEG functional groups at the surface forming dipoles able to interact with counterions or water dipoles [49]. Loading LNCs with 10 and 100 μM Hy did not affect the zeta potential values revealing complete encapsulation of lipophilic Hy in the oily core of LNCs. However, the loading of 200 μM Hy into LNCs (Hy-LNCs 3) showed the highest negative zeta potential value (−12.25 ± 2.43), indicating that Hy encapsulation, in this case, could be attributed to entrapment in both the Labrafac® oily core and the lipophilic domains of Lipoid® S 100 in the shell of LNCs. Specifically, the preferential localization of Hy in lipid membranes of giant unilamellar vesicles was proven earlier [21,50]. Similar observations were recorded with amiodarone and quercetin, where the drug was preferentially arranged at the oil phase/surfactant PEG moieties interface of surfactant [51,52].

3.1.2. Transmission Electron microscope studies

To get an insight into the morphology of the Hy-LNCs, samples of the fabricated formulations were visualised using TEM. The recorded micrographs showed spherical uniformly distributed Hy-LNCs with particle size in accordance with the size measurements recorded by dynamic light scattering analysis. (Fig. 2c).

3.1.3. Drug content and entrapment efficiency determination

LNCs are known to have too high capabilities to encapsulate and solubilize different hydrophobic anticancer drugs, such as paclitaxel and docetaxel, as well as photosensitisers, such as hypericin and protoporphyrin [22,53,54]. In the present work, loading of LNCs with the hydrophobic Hy resulted in remarkably high EE% that ranged between 89.64 ± 0.44 and 100% ± 0.03. The achieved EE% values were higher than those reported in previous studies, whereas EE of 75% and 80% were obtained when Hy was encapsulated into polycaprolactone-poly (ethylene glycol) and solid lipid nanoparticles, respectively [5,16,17]. In addition, the prepared Hy-LNCs achieved reliable drug content that ranged between 98.16% ± 2.47% and 100% ± 3.72%, indicating homogenous drug distribution within the formulations.

3.1.4. Photodynamic activity measurement

The photodynamic efficiency of free Hy (as a control) and Hy-LNCs was assessed by determining the rate constant for the photodecomposition of uric acid (UA) as a singlet oxygen scavenger and a chemical dosimeter [36]. Uric acid (UA) a known singlet oxygen scavenger, was utilized as a chemical dosimeter for determining photodynamic activity in the PDT through a quenching mechanism. Therefore, the decomposition constant and the reduction in UA absorbance band at 292 nm after light irradiation in the presence of photosensitiser are related to the production of singlet oxygen ($^1O_2$) and provides rapid evaluation of $^1O_2$ relative formation by the photosensitiser. The optimal UA concentration and the maximum irradiation time were determined based on preliminary experiments (data not shown) that was also in agreement with the observations of other workers [18,55].

As shown in Fig. 3a, pure UA in PBS pH 7.0 with 0.001% Tween 20, free of Hy, showed no decrease in absorbance at 292 nm and had no absorption bands in the emission wavelength of the light source (595 ± 10 nm and 27.38 ± 3.45 mW cm^{-2}) indicating that there was no interaction between UA and the light, as this interaction was restricted to the photosensitiser.

As shown in Fig. 3c, d and e, the absorption intensity of UA in the presence of Hy-LNCs decreased gradually as a function of time under irradiation by the LED. In contrast, the change in the absorption intensity was insignificant in the case of Hy solution (Fig. 3b).

Moreover, based on the UA test, the rate constants of photooxidation (K) of UA were determined (Fig. 3f and g). Encapsulation of Hy in three different concentrations in LNCs significantly (One-way ANOVA, $P < 0.0001$) improved its photoactivity. The K values for Hy-LNCs 1, Hy-LNCs 2, Hy-LNCs 3 and Hy solution were 32.00 × 10^{-3} ± 1.13, 58.50 × 10^{-3} ± 2.96, 37.40 × 10^{-3} ± 0.28 and 0.93 × 10^{-3} ± 0.35 min^{-1} respectively. The Hy-LNCs formulations showed 35, 65, and 41 fold increase in rate constants for the decomposition of UA, respectively, compared to Hy in solution.

Additionally, the photodynamic activity (PA) of the three Hy-LNCs formulations was compared (Table 2). After 30 min of light irradiation at 595 ± 10 nm and 27.38 ± 3.45 mW cm-2, the PA achieved 125, 396 and 438 fold increases for Hy-LNCs 1, Hy-LNCs 2, Hy-LNCs 3, respectively, compared to Hy solution. As reported earlier, Hy exhibits low aqueous solubility, causing it to self-aggregate by building hydrogen bonds to other Hy molecules through the carbonyl and the phenolic hydroxyl groups leading to stacked homoassociates. These aggregated units reduce the quantum yield and the lifetime of the excited triplet state of PSs due to self-collision, and consequently, the $^1O_2$ generation yield should be reduced [56,57]. This explained the negligible change in the absorption intensity of UA after irradiation and the very weak ROS production in the case of Hy solution.

Interestingly, the ROS were generated more efficiently in Hy-LNCs than Hy solution. One can deduce that the Hy-LNCs inhibited the aggregation of Hy and consequently, the triplet state has a longer lifetime, suggesting that Hy-LNCs have greater photodynamic activity than free Hy. Similar results were reported when Hy was loaded into solid lipid and polycaprolactone-poly (ethylene glycol) nanoparticles [17,18]. Besides, the same phenomenon was observed with protoporphyrin IX-loaded silica spheres [58]. Thus, the achieved increase in quantum efficiency could be a consequence of a decrease in dimer formation due to Hy-loaded LNCs.

The PS concentration is critical to avoid saturation and self-quenching effect [59,60]. The Hy-LNCs 2 with intermediate drug loading achieved the highest K (58.50 × 10^{-3} ± 2.96 min^{-1}) and the highest PA (59.43 ± 0.28 m^2/J). In other words, the ROS production increased by increasing the Hy loading in LNCs from 10 to 100 μM, however, a significant decline in both the ROS and the PA were observed with the highest, 200 μM, drug loading. A possible explanation could be that increasing Hy loading in the particles promoted liability to aggregation and accordingly decreased the triplet state lifetime and reduced the generated ROS [16,17]. However, again there was no visual nor microscopic evidence for aggregation. Another possible explanation could be that higher drug loading gives rise to more compact structures so part of the drug became readily not available for PDT [16].

Generally speaking, the efficiency of PDT can be attributed to the production of $^1O_2$, so oxygen diffusion is crucial when considering nanocarriers-loaded photosensitisers [61]. It has been proven that LNCs allow oxygen to diffuse freely in and out of the system [62]. Considering that ability for free oxygen diffusion side by side with the observed results for PA and ROS production in our study, LNCs appear a promising DDS for modulating the ROS generation of photosensitisers.

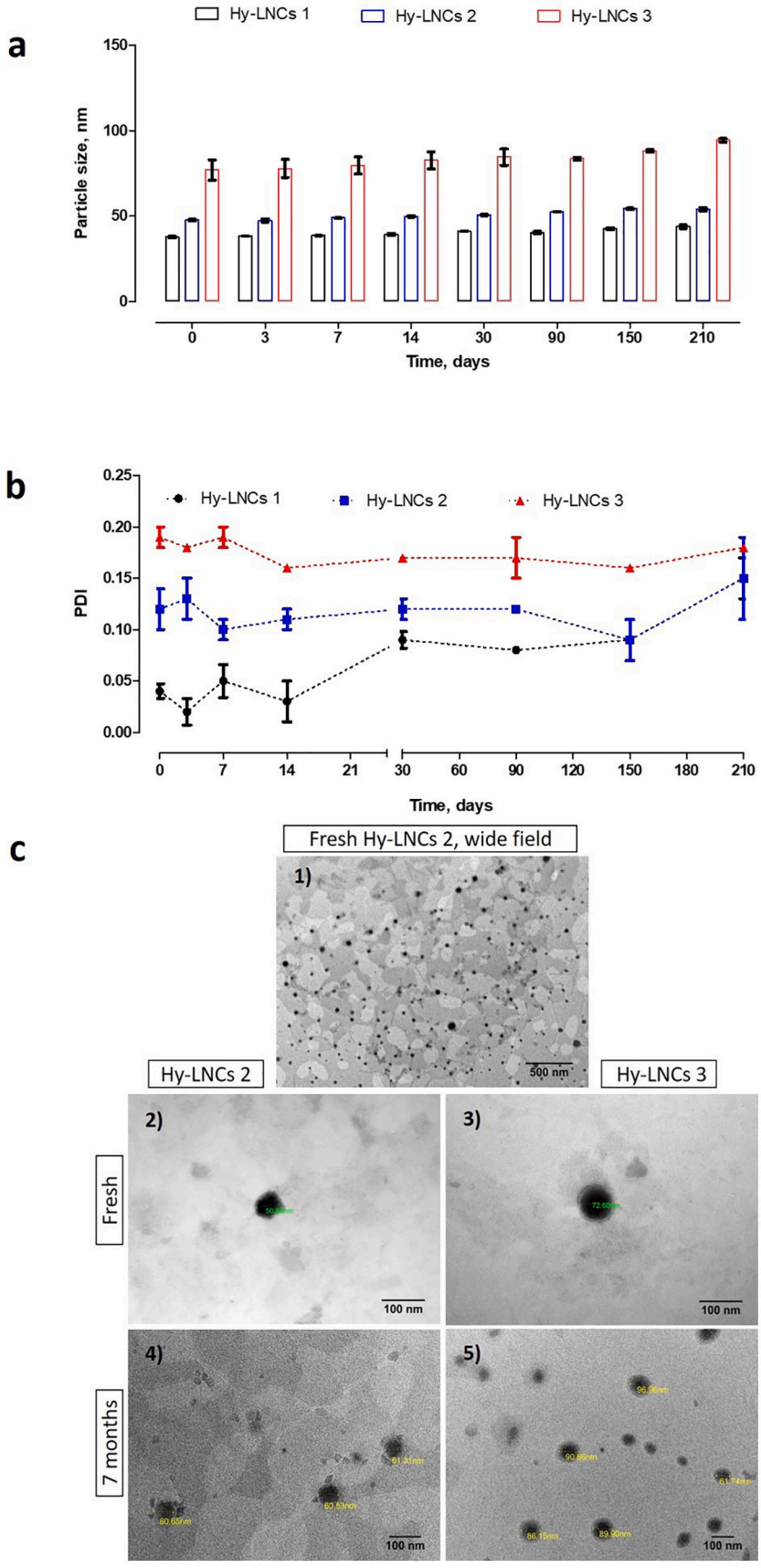

Fig. 2. **a)** Particle size and **b)** polydispersity index (PDI) profiles of different Hy-LNCs formulations throughout 7 months storage at 2–4 °C. Non-significant difference within the same formulation throughout storage (One-way ANOVA with Tukey's multiple comparison *post hoc* test, $p < 0.05$). **c)** TEM images of: Freshly-prepared and 7 months-stored Hy-LNCs 2 & Hy-LNCs 3 at magnification powers of 15 K, 80 K, 80 K, 60 K and 40 K, respectively. Data reported as mean ± SD, n = 3.

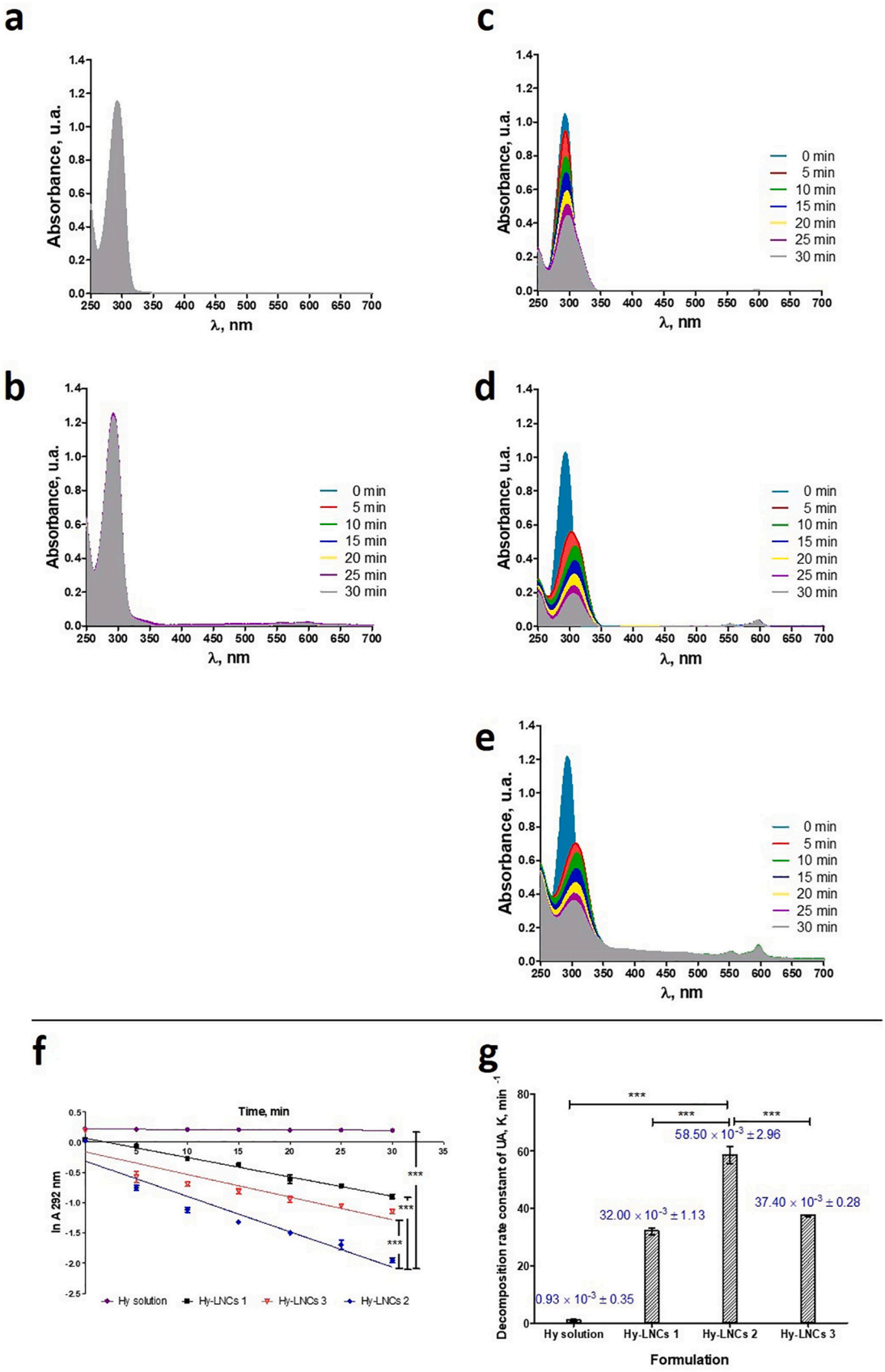

Fig. 3. UV spectra of a) uric acid (UA), b) Hy solution, c) Hy-LNCs 1, d) Hy-LNCs 2, e) Hy-LNCs 3 throughout 30 min irradiation and f) & g) the decomposition rate constants of the three formulations in comparison to the control solution. ***Highly significant difference from Hy control solution (One-way ANOVA with Tukey's multiple comparison *post hoc* test, $p < 0.0001$). Data reported as mean ± SD, n = 3.

Table 2
Photodynamic activity (PA) and n fold increase in PA of different Hy-LNCs formulations compared to Hy solutions of the same concentrations. Data reported as mean ± SD, $n = 3$.

Formulation	Hy Conc. (μM)	PA (m^2/J)	PA of corresponding Hy solution	n fold increase in PA
Hy-LNCs 1	0.2	31.29 ± 6.06	0.25 ± 0.05	125
Hy-LNCs 2	2	59.43 ± 0.28	0.15 ± 0.06	396
Hy-LNCs 3	4	21.90 ± 0.59	0.05 ± 0.01	438

Measurement conditions: [UA] = 1.8×10^{-4} mol L^{-1}, irradiation wavelength (λ_{irr}) = 595 ± 10 nm, irradiation time = 30 min, fluence rate = 273.84 ± 34.59 W/m^2.

3.1.5. Photostability determination

Photoirradiation of Hy DMSO solution and Hy-LNCs 2 Samples of equivalent concentrations was done using a LED at 595 ± 10 nm and 27.38 ± 3.45 mW cm^{-2} as fluence rate. The percentage of degraded Hy was estimated at 0, 10, 20, 30 and 40 min using HPLC analysis at 590 nm. As shown in Fig. 4, photoirradiation of Hy DMSO solution inflicted 53% degradation in the first 10 min. Further irradiation-induced complete drug photodegradation, nearly 100% of Hy was degraded at 20 min. Under the same conditions, the encapsulation of Hy into LNCs significantly enhanced its photostability and reduced its photodegradation, compared to free Hy in DMSO solution (Student's *t*-test, $P < 0.0001$) as only 18% of Hy-LNCs underwent photodegradation after 40 min of irradiation.

Lima and colleagues [18] studied the photodegradation of free and entrapped Hy in solid lipid nanoparticles, observing 37% and 18.5% photodegradation for free and loaded Hy, respectively, after 40 min irradiation at 590 ± 10 nm and $I = 10$ mW cm^{-2}. Similarly, Youssef and colleagues [5] recorded 15.6% photodegradation for free Hy compared to only 6% photodegradation for Hy loaded in solid lipid nanoparticles after 35 min irradiation at 550 ± 10 nm and $I = 80$ mW cm^{-2}.

The ability of LNCs to protect their cargo against photodegradation has not been extensively studied in the literature. However, LNCs significantly improved the photostability of curcumin, as proven by Mazzarino, et al. [63]. Such capability for photoprotection is a consequence of the size, shape and vesicular core-shell structure of the nanocapsules [64]. Moreover, LNCs, as colloidal carriers, seems to modulate the photophysical properties of Hy, such as prolongation of triplet state lifetime and enhancement of its optical absorption [18]. This could have an influence on reducing the photodegradation of encapsulated Hy.

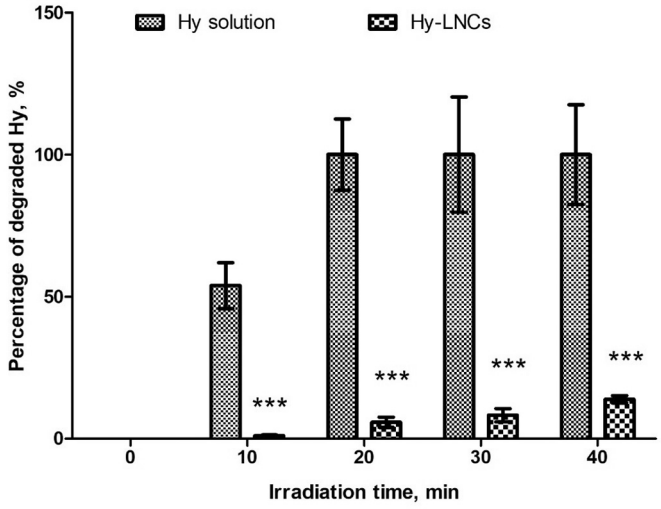

Fig. 4. Percentage of degraded Hy before and after irradiation with a LED of 595 ± 10 nm, $I = 273.84 \pm 34.59$ W/m^2 for time intervals of 0, 10, 20, 30 and 40 min of Hy and Hy-LNCs 2. ***Highly significant difference from Hy control solution (Student's *t*-test, $p < 0.0001$). Data reported as mean ± SD, $n = 3$.

The obtained improvement in the photostability of Hy in LNCs indicates that the drug has been most likely embedded in the LNCs matrix rather than being adsorbed. These results suggest that LNCs exhibit an encouraging potential to enhance the photostability of Hy.

3.1.6. Evaluation of Hypericin cellular uptake and photocytotoxicity

The cellular uptake is the key prerequisite for characterizing the photodynamic effect of Hy on cellular viability. Therefore, cellular internalization of free and nano-encapsulated Hy was evaluated visually by confocal microscopy imaging and quantitively by flow cytometry after 2 h incubation with the mouse melanoma cell line (B16-F10). The determination of the optimal time slot for cells irradiation and thus Hy photoactivation is very important. Therefore, the 2 h time point was selected based on preliminary studies as the time point of choice for optimum cell uptake. Data showed that melanoma cells should be incubated with the photosensitiser Hy for 1.5 to 2 h before irradiation to gain maximum photodynamic action of Hy on the viability of the intended cancer cells. This was in agreement with previous studies where Hy accumulated in EMT6 mouse carcinoma cells in 2 h [65]. The behaviour of blank and loaded LNCs in the culture medium was checked microscopically and no aggregation was detected, indicating the good stability of LNCs.

Based on the confocal images (Fig. 5), DAPI staining showed that cell nuclei were well counterstained with DAPI. Furthermore, all Hy-LNCs treated cells showed bright red intracellular fluorescence. These observations demonstrated that Hy-LNCs accumulated in multiple subcellular domains in B16-F10 melanoma cells achieving efficient Hy-LNCs uptake. In fact, this subcellular localization pattern of Hy was also reported in different cell types where Hy and/or Hy-loaded nanoparticles were not only bound to the plasma membranes but also accumulated in the membranes of the endoplasmic reticulum and Golgi apparatus [13,21,65].

In parallel, a quantitative evaluation of the cellular uptake of different Hy concentrations in solution form and LNCs using flow cytometrical analysis in dark and light (595 ± 10 nm, $I = 273.84 \pm 34.59$ W/m^2) conditions was performed. The fluorescence intensity% was considered as a parameter reflecting the cellular uptake of Hy into B16-F10 melanoma cells. Fig. 6a represents the fluorescence intensity% plotted against different concentrations of Hy in solution form and LNCs before and after irradiation.

Throughout the full tested concentration range (0–3 μM) of the drug, Hy-LNCs exhibited significantly (One-way ANOVA with Tukey's multiple comparison *post hoc* test, $p < 0.05$) higher fluorescence intensity% relative to Hy solution reflecting increased cellular uptake for the encapsulated Hy. Light irradiation had no significant effect on the cellular uptake of free or nanoencapsulated Hy into melanoma cells.

The mechanism of photosensitiser cellular uptake influences their intracellular localisation and, ultimately their photodynamic activity. Encapsulation may thus modify subcellular distribution of photosensitisers into the different compartments of the cell. Free lipophilic Hy, in solution form, generally can cross plasma membranes by diffusion, leading to a low intracellular accumulation. On the contrary, LNCs, as intracellular drug vehicles for cancer cells, are taken up by endocytosis leading to the higher intracellular concentration of an entrapped drug. Therefore, the various cellular uptake pathways of photosensitiser could be rate-depending whether it is free or encapsulated [16,66,67].

The first and foremost step in the development of an anticancer formulation is to evaluate its inhibitory action against the viability of cancer cells. To explore the potential anticancer photodynamic application of Hy-LNCs, MTS colorimetric assay in mouse melanoma cells (B16-F10) treated with Hy and Hy-LNCs (0.1–5 μM Hy corresponding to 1.12–56 mg/ml LNCs) in dark and light conditions was performed. The

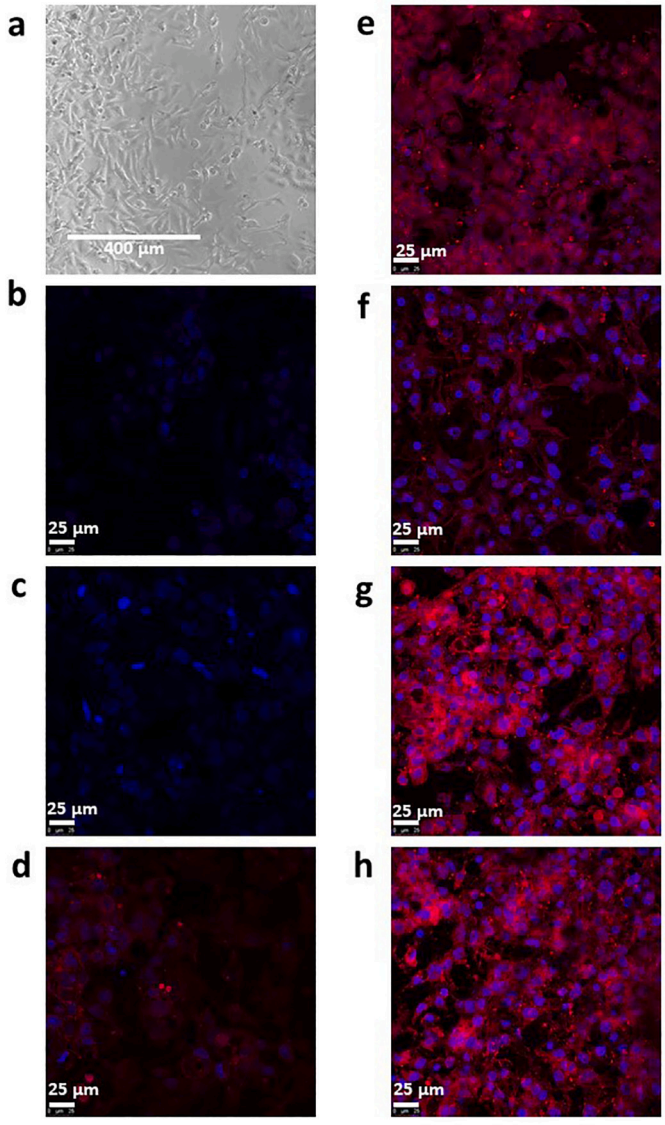

Fig. 5. a) Digital image of mouse melanoma cells (B16-F10). Confocal fluorescence images of; **b)** control cells, 2 h incubation alone **c)** with blank LNCs, with **d)** 0.2 µM, **e)** 0.4 µM, **f)** 0.6 µM, **g)** 0.8 µM and **h)** 1 µM Hy-LNCs 2. Blue colour indicates the DAPI staining cellular nuclei and red colour represents the Hy. Data reported as mean ± SD, $n = 3$. (For interpretation of the references to colour in this figure legend, the reader is referred to the web version of this article.)

B16-F10 line was selected in this *in vitro* study as melanoma is known to be the most resistant to PDT among skin malignancies due to the presence of large amounts of light-absorbing melanin pigment. Fig. 6b shows the changes in cell viability triggered by different treatments in the presence and absence of light.

Dark controls (untreated cells) and positive controls (irradiated untreated cells) revealed a normal cell culture without loss of cell viability. In the absence of photoactivation, there was a negligible difference (One-way ANOVA, $P > 0.05$) in the viability of Hy solution treated and untreated cells throughout the concentration range (0.1–3 µM). Cell survival was >97% except for the highest concentration (5 µM), which showed small cytotoxicity with 83% cell survival. The exerted low dark toxicity of Hy solution was in line with the low ROS previously generated in the dark. After photoactivation, Hy solution inhibited the viability of melanoma cells in a concentration dependant manner. The IC_{50} was equal to 0.8 µM and the lowest cell viability was reached at 5 µM. As reviewed by Karioti and Bilia [68], light activation is mandatory for the expression of cytotoxic activity of Hy. Briefly, the ROS released from photoactivated Hy provoke apoptosis and necrosis by initiating loss of plasma membrane integrity, the disintegration of the endoplasmic reticulum, Golgi apparatus and mitochondria leading to cell death [13].

Hy-LNCs, in dark conditions, showed an IC_{50} of 1.5 µM and minimum cell viability at 3 µM. While the irradiated Hy-LNCs recorded the IC_{50} at only 0.2 µM and the maximum cell killing was reached at 0.4 µM. The data clearly revealed that Hy-LNCs photoactivation potently reduced the melanoma cells proliferation starting from concentrations as low as 0.2 µM. Hence, the irradiated Hy-LNCs showed significantly higher cytotoxicity compared to irradiated Hy solution. It is known that Hy suffers from intracellular aggregation leading to quenched fluorescence and hampered phototoxic effect on cells [16]. Interestingly, the prepared LNCs prevented the intracellular aggregation of Hy and triggered highest photocytotoxicity and best cell death activity in light conditions.

Previously, Hy-loaded nanocapsules exerted a dose-dependant cytotoxic effect on human cervix carcinoma ($IC_{50} = 0.62$) and human breast adenocarcinoma ($IC_{50} = 0.56$) cells [22]. Similarly, the observed Hy solid lipid nanoparticles phototoxicity on HEp-2 and B16–F10 cell lines proportionally increased with drug concentration [18]. On the contrary, the potency of the prepared Hy-LNCs in the current study outperformed the concentration-dependant pattern observed with Hy solution and other Hy nano-systems in previous studies.

In order to clearly understand how the nanocarriers themselves affect cells. The influence of a wide range of B-LNCs concentrations (1.12–56 mg/ml) as a primitive step of studying their potential use as anticancer photodynamic drug delivery vehicles was investigated, Fig. S3. In the concentration range (0–5.5 mg/ml), B-LNCs showed a safe toxicity profile with 100–88% cell viability. At 11.5 mg/ml, the viability reduced to 75% and the lowest exerted viability (65%) was reached at 56 mg/ml of LNCs. In comparison to Hy-LNCs at dark and light conditions, data showed that there was a significant (One-way ANOVA with Tukey's multiple comparison *post hoc* test, $p < 0.05$) difference between the B-LNCs and photoactivated Hy-LNCs toxicity profiles in favour of the loaded nanocarriers indicating that the most prominent effect on cancer cell death was due to the irradiated encapsulated Hy rather than the system itself.

Only a few studies have discussed the cellular uptake and cytotoxicity of low concentrations of B-LNCs (0.1–1 mg/ml) [79,80,83]. Szwed, and colleagues [66] demonstrated that endocytosed empty LNCs ended up in lysosomes causing a reversible inhibitory effect on protein synthesis, increase in lysosomal pH and acidification of cytosol. Moreover, LNCs were able to alter cellular redox homeostasis and induce ROS production, causing oxidative stress associated with subsequent lipid peroxidation and membrane damage.

It is worth mentioning that LNCs-induced cell death, at high concentrations, on different cell lines was mainly ascribed to Solutol® HS 15 [69]. Many hypotheses were assumed to explain that effect. Some attributed the toxicity to the surfactant amphiphilic structure that enables for interaction with polar head groups and lipophilic tails of cellular lipid bilayers causing a disruption of the plasma membranes. Others linked the observed toxicity to the chemical nature of the non-ionic surfactant and the length of the hydrophilic PEG chain [69]. However, the exact mechanism behind this toxic effect has not yet been revealed.

It is noteworthy that not all nanocarrier-based delivery systems improved cellular uptake and cytotoxicity of photosensitisers. Encapsulation of Hy into solid lipid nanoparticles diminished both cell uptake and mortality [5]. Thus, LNCs are more advantageous over other nanoparticles as a photodynamic anticancer drug delivery system. According to previous studies, the Hy subcellular localisation critically defies its phototoxicity [13]. In other words, the major role of LNCs, in the presented system resides in enhancing Hy solubility in biological conditions, preventing aggregation, facilitating its cellular uptake and

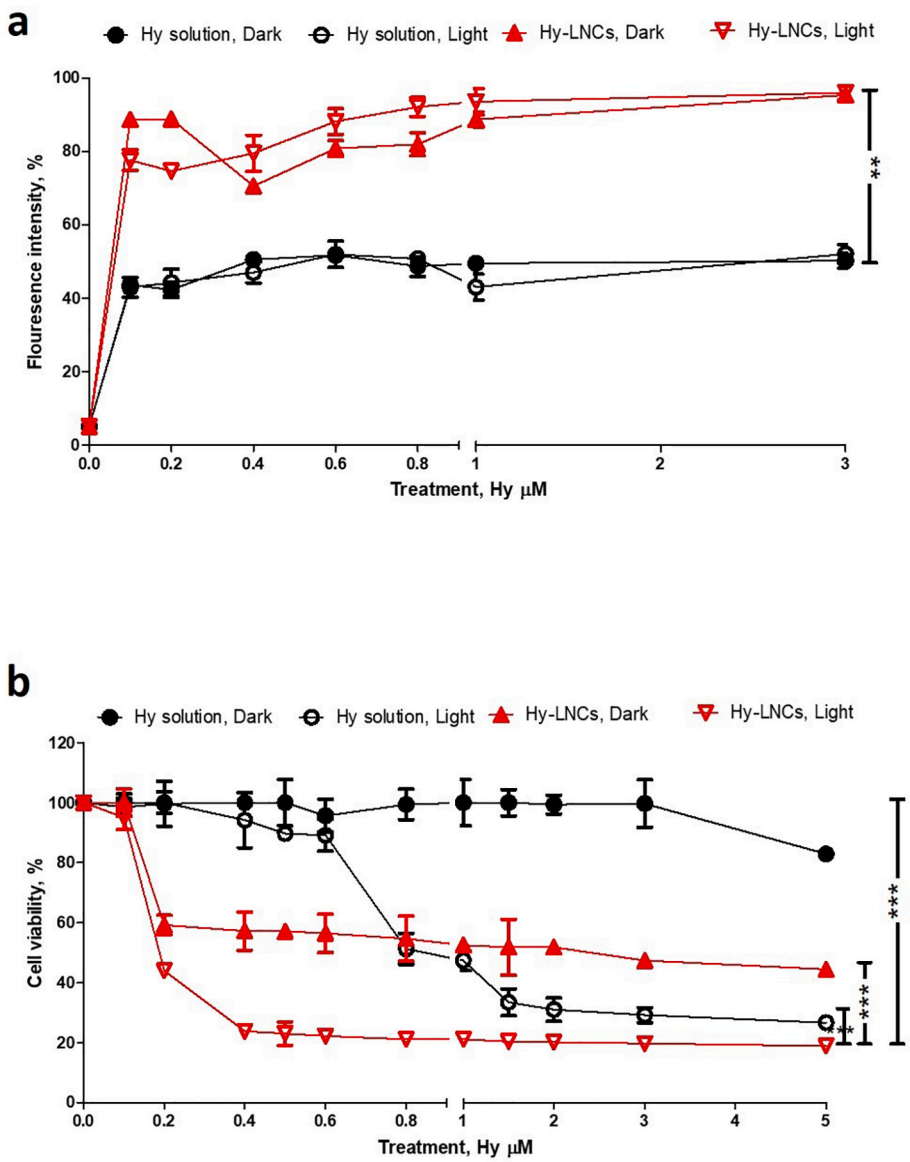

Fig. 6. a) Percentage of fluorescence intensity due to uptake of Hy into B16-F10 mouse melanoma cells from Hy-solution and Hy-LNCs 2 in dark and light (595 ± 10 nm, $I = 273.84 \pm 34.59$ W/m^2) conditions for different concentrations. **b)** Cell viability assay (MTS test) for B16-F10 mouse melanoma cells after 24 h incubation with different concentrations of Hy solution and Hy-LNCs. ***Highly significant difference from other profiles (One-way ANOVA with Tukey's multiple comparison *post hoc* test, $p < 0.0001$).

its subsequent photodynamic activity.

Collectively, the significantly potent Hy-LNCs-induced cell death could be attributed to a combined synergistic effect between Hy, LNCs and light. Therefore, nanoencapsulation favours Hy internalization and thus, its cellular photoactivity.

3.1.7. *Stability evaluation*

Long-term physical stability of Hy-LNCs was carried out to ensure that there is no aggregation or drug leakage upon storage since particle diameter and drug content are crucial factors in stability. Thus, Hy-LNCs shape, particle size, PDI, zeta potential, EE% and DC% were evaluated at pre-determined time intervals over 7 months. The prepared Hy-LNCs maintained their spherical morphology and monomodal particle size distribution without significant difference for 7 months when stored at 2–4 °C in dark conditions (Fig. 2). The particle size of Hy-LNCs 1 and Hy-LNCs 2 was 37.77 ± 0.41 and 47.76 ± 0.49 nm at 0 times compared to 43.83 ± 1.18 and 54.02 ± 1.00 nm at 7 months. PDI remained below 0.15 during the whole period. Except for Hy-LNC 3, the highest drug level, at 7 months of storage where the particle size increased significantly (One-way ANOVA, $P < 0.05$) to 94.37 ± 1.06 nm compared to 76.88 ± 5.95 nm for fresh formulation. This could be attributed to micro aggregation of the excess drug. However, there was neither visual nor microscopic evidence of aggregation.

Moreover, within each formulation, there was no significant change in the slightly negative zeta potential values throughout the storage period as expected due to the shielding effect and steric stabilization exerted by the PEG chains in the shells of LNCs, Fig. S1 [48].

From the same point of view, the results of the stability study (Fig. S2) highlighted stable EE% and DC% without drug leakage over 7 months of storage. This suggested that Hy remained buried inside the LNCs.

3.2. *Evaluation of microneedles-assisted delivery of Hypericin-loaded lipid nanocapsules using hollow microneedles*

Skin is presumed to be a formidable barrier to the penetration of large molecular size therapeutics [70]. Based on preliminary studies, the intradermal delivery of Hy loaded in LNCs were limited to the superficial layers of the skin and could not penetrate beyond *the stratum corneum (SC)* in considerable amount in 2 h. That was in line with previous reports, where LNCs accumulated on the skin surface, including the hair follicle spaces without penetration into deeper skin layers after dermal

application [23,24]. Therefore, there was an unmet necessity for the use of the intradermal delivery system to overcome the skin barrier properties and enable deep skin delivery.

MNs are micron-scale needles with the potential to deliver molecules and macromolecules across the skin without causing significant pain [71]. So far, several research groups have studied the delivery of particulate systems utilizing MNs *via* the transdermal route [72–74]. Thereby, MNs represented a promising candidate to achieve intradermal delivery of Hy-LNCs.

Ho-MNs are MNs that create aqueous micro-channels through which the drug formulation can be infused [75]. These MNs enable direct drug deposition into the viable epidermis or the dermis avoiding the *SC* [76]. In the present study, two types of Ho-MNs (AdminPen™ and S-Ho-MN) were investigated for their capabilities to pierce excised porcine skin to create intradermal microconduits and further efficiency for *ex vivo* intradermal delivery of Hy-LNCs.

The AdminPen™, 1200 μm, is a non-invasive and painless intra/transdermal delivery device that is based on the patented proprietary Ho-MN array technology called AdminPatch MN array, covered by US Patent No. 7,658,728 [77]. The novel MNs-based AdminPen™ Ho-MNs consists of very sharp 43 stainless steel MNs of 1200 μm length and 1 cm square area of circular MNs array (Fig. 1). When connected to a standard syringe, AdminPen™ Ho-MNs can deliver liquid formulations into the skin. The MNs array instantaneously forms hundreds of tiny micropores through the *SC* and epidermis. The created aqueous channels had a depth of about 1100 to 1200 μm, sufficient to extend through the viable epidermis into the dermis to reach blood capillaries but shallow enough to avoid most pain receptors. The AdminPen™ Ho-MNs is characterised by having off-centred hollow shaft on the side of each MN, this innovative design was reported to secure sustained and efficient drug delivery without cloggage [76]. After removing the MNs array from the skin, the micropores simply collapse and the skin barrier is quickly restored [76].

Despite AdminPen™ system was introduced to the market approximately 10 years ago, it was successfully used for dermal and transdermal delivery of different drugs and formulations including; microparticulate interleukins vaccine for ovarian cancer [78], iron-dextran colloidal solution for iron replenishment [79], vismodegib for the treatment of basal cell carcinoma [80], the antimicrobial carvacrol loaded polycaprolactone nanoparticles [54], and was also used for the detection of glucose and rhodamine 6G [81].

Based on the previously adopted approach that Ho-MNs can be fabricated from commercially available hypodermic needles [82]. Usually, the gauge needles were cut to the desired length and glued to premanufactured moulds [83]. In the present study, the in-house S-Ho-MN, was fabricated by mounting a PLA 3D-printed holder to a 26G × ½ inch stainless steel Terumo® needle (Fig. 1). The developed MN shaft was 1340 μm in length [84]. The engagement of 3D-printed holders rather than conventional metallic or polymeric moulds offered several advantages, including ease of fabrication, short production time, high accuracy and no harmful hazard.

The porcine tissue was chosen for the *ex vivo* tests because it was specifically considered as a representative model for human skin due to morphological and functional similarities [85].

3.2.1. Insertion properties assessment

The efficient insertion of MNs into the skin is critical to its use, as the SC must be penetrated by the MNs to exert their effects. Therefore, the insertion capability of the AdminPen™ Ho-MNs and S-Ho-MN through Parafilm M® and full-thickness excised neonatal porcine skin was evaluated as an integral part of the MN-based system assessment.

The AdminPen™ Ho-MNs succeeded in recording 100% penetration in the first five Parafilm M®, >48% in the sixth layer, and > 43% in the seventh layer. This means that MNs penetrated up to 889 μm depth (the seventh layer), corresponding to 80.8% of the actual needle length. According to Larrañeta et al. [86], the production of >20% holes in each layer is sufficient to ensure successful MNs insertion. AdminPen™ Ho-MNs clearly exceeded this percentage in every layer. Fig. 7d is a representative graph of the percentage of microholes created in each parafilm layer. In the same context, S-Ho-MN achieved up to 1294.8 ± 16.9 μm penetration in the Parafilm M® membrane reaching the eleventh layer reflecting penetration of >95% of the actual needle length, as provided in the OCT image in Fig. 9I.

Both MN systems were mechanically strong enough to penetrate the full thickness excised neonatal porcine skin. The AdminPen™ Ho-MNs achieved 100% penetration, as shown in the digital microscope image, Fig. 7a. The microholes created by each MN in the array were clearly defined, 43 micropores in total, with interspacing distance in accordance with the tip-to-tip MNs distance on the array. As shown before, this reflected that the created micropores were due to the MNs sharpness, and the substrate of the array did not disturb the barrier function of the *SC* [80]. The MNs were then easily removed without any bending or damage. The MNs penetrated through a depth of 1045.5 ± 22.8 μm, as shown in the OCT image of the punctured excised skin in Fig. 7b, recording a penetration depth of approximately 95% of the actual needle length.

Consequently, these data indicated that AdminPen™ Ho-MNs and S-Ho-MN were mechanically strong to efficiently penetrate the skin barrier. Hence, the proposed MN-based delivery systems showed a promising potential for application to cancerous and/or hyperkeratotic skin lesions.

3.2.2. Pore closure kinetics

To the best of our knowledge, this is the first study to report the pore closure kinetics after AdminPen™ Ho-MNs insertion to the skin. The sterile nature of AdminPen™ Ho-MNs and the rapid recovery of skin barrier properties were critical to avoid any possible skin infection. Sterility of AdminPen™ Ho-MNs was guaranteed by the manufacturer. Thus, the time required for complete pore closure was monitored by recording OCT images every 2 min for the porcine skin after removal of AdminPen™ Ho-MNs, Fig. 7c. The healing process was rapidly initiated at 2 to 4 min and complete restoration of skin barrier properties was observed at 10 min. These results were supported by other studies where short duration MN treatment time (< 4 min) led to rapid skin contraction and microchannels closure due to inherent skin elasticity [80,87].

3.2.3. Ex vivo dermatokinetic studies

Since the primary aim of the present study was to deliver Hy-LNCs into the deeper layers of skin, the loaded LNCs were injected into full-thickness excised neonatal pig skin using AdminPen™ Ho-MNs injector and S-Ho-MN systems where the Hy-LNCs were allowed to seep through the microchannels created by the Ho-MNs in the skin. The created aqueous channels constantly remained open while the AdminPen™ Ho-MNs array or the S-Ho-MN was being applied on the skin, and therefore enabled the rapid, free-flowing, sustained, and efficient delivery of Hy-LNCs through these aqueous channels formed in the skin surface. The distribution of Hy-LNCs within the skin tissue, following the Ho-MNs application, was visually indicated with the reddish colour of the tissue (Fig. S4). No needle blockage was observed, and the formulation remained confined within the skin layers without any leakage. When the MNs were removed from the skin, the micropores simply collapse, and the skin barrier is quickly restored.

The skin distribution of Hy / Hy-LNCs in different layers of full-thickness porcine skin was then quantitively assessed per cm^3 and after 1 h of AdminPen™ Ho-MNs application. Hy was extracted from the skin using acetonitrile before being analysed using the HPLC method, as described in Section 2.5. The amount of Hy, expressed in μg, deposited at different depths of skin for both Hy solution and Hy-LNCs are illustrated in Fig. 7e. At each depth level, loaded LNCs fulfilled significantly (Student's t-test, $p < 0.0001$) higher Hy amount relative to drug solution. Moreover, Hy was distributed within the excised tissues up to a depth of 2900 μm for Hy-LNCs compared to only 900 μm for Hy in solution form.

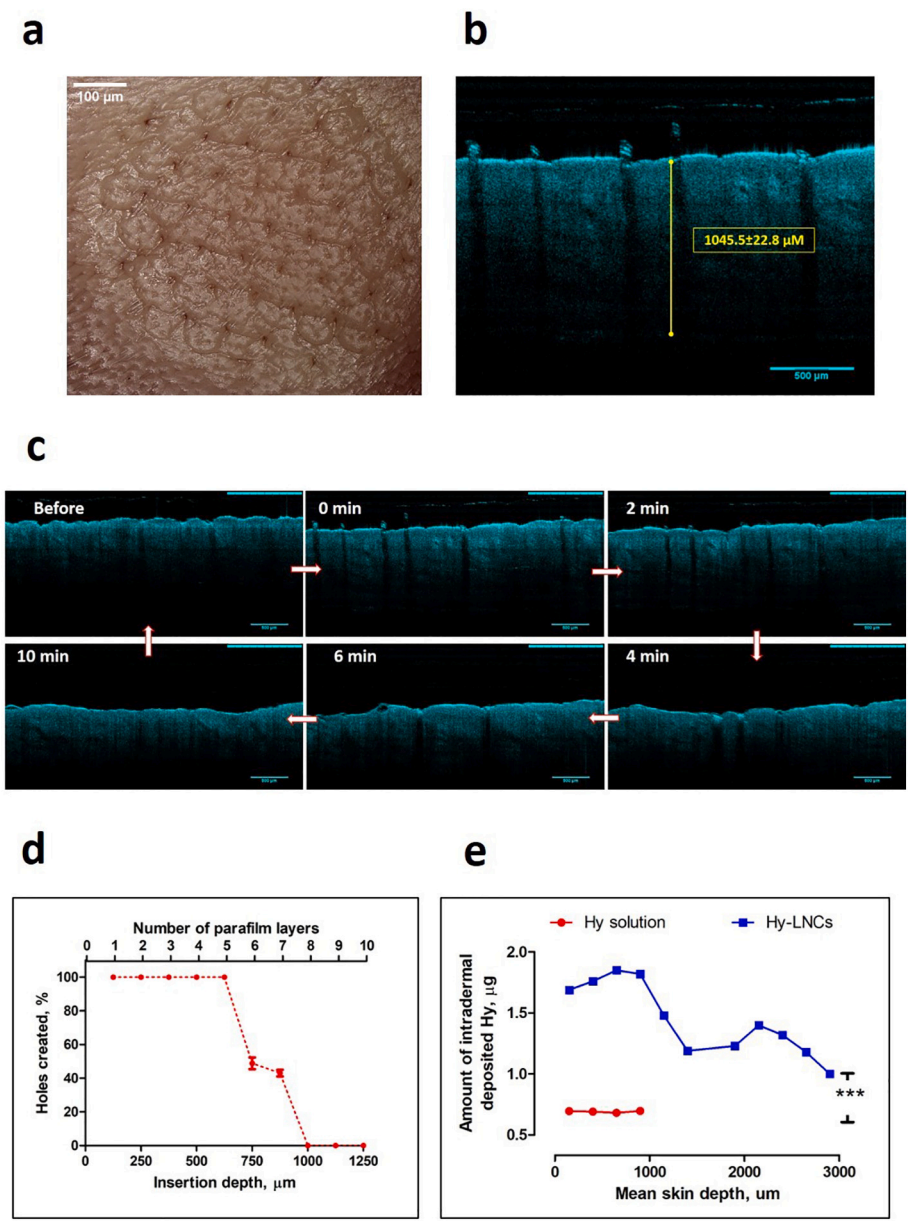

Fig. 7. **a**) Digital microscope image, **b)** OCT image of excised neonatal porcine skin after insertion of AdminPen™ 1200 µM Ho-MN array. **c)** OCT images recording the pore closure and skin recovery process after insertion of AdminPen™ Ho-MNs into excised neonatal porcine skin, scale bar represents 500 µm. **d)** Percentage of microholes created in each parafilm layer during MNs insertion assessment, **e)** *Ex vivo* skin distribution study of Hy solution and Hy-LNCs 2 across excised full-thickness neonatal porcine skin after injection using AdminPen™ Ho-MNs quantified by cryostat sectioning. Injected Hy amount was 25 µg. ***Highly significant difference from Hy control solution (Student's *t*-test, $p < 0.0001$). Data reported as mean ± SD, $n = 3$.

These results revealed that encapsulated Hy was detected at a depth greatly exceeding the height of MNs (1100 µm), reflecting the movement of drug particles in the skin.

In addition, following the administration through AdminPen™ Ho-MNs, the cumulative amount of Hy deposited in the skin from LNCs was found to be 16.80 µg (≈ 75% of the administered dose) compared to only 2.76 µg (12% of the administered dose) for free Hy. Therefore, the application of Hy-LNCs using Ho-MNs could lead to substantial amounts of Hy across the skin.

From the same point of view, the total skin deposition of free and encapsulated Hy was examined per cm^3 at different time points after S-Ho-MN injection. Figure 9III, represents the *ex vivo* total intradermal deposited amounts of Hy from solution and LNCs across excised full-thickness neonatal porcine skin after injection using S-Ho-MN. Again, LNCs accomplished a significantly high deposited amount of Hy (23.11 µg ± 0.59 ≈ 92.5% of the administered dose) compared to negligible in-skin drug deposition for free Hy solution (3.51 µg ± 0.01 ≈ 14% of the administered dose) at each time point. Prolonged skin exposure (0.5 to 6 h) did not affect the observed deposited ratio in favour of the LNCs.

In order to visualize the fluorescent Hy intradermal distribution from solution and LNCs after AdminPen™ Ho-MNs application, confocal images were captured for transverse and longitudinal skin slices after cryostat sectioning, Fig. 8. The z-stack was conducted for longitudinal skin sections to clarify the depth that the drug could reach in the skin in the case of Hy-LNCs, as presented in Figure 8II. Similarly, to detect the Hy distribution within the full-thickness excised neonatal porcine skin following S-Ho-MN injection, multiphoton fluorescence images were recorded, Fig. 9II.

The fluorescence intensity is a good indication for the amount of solubilized Hy [14]. Thus, according to confocal and multiphoton images, weak fluorescence in skin samples treated with drug solution reflected low solubility and poor in-skin Hy distribution. In contrast, the images of skin tissues treated with Hy-LNCs showed stronger fluorescence intensity. This phenomenon reflected that LNCs clearly enhanced the extent and depth of Hy distribution within the skin. The significantly higher fluorescence intensity in the case of Hy-LNCs could be attributed to the fact that Hy is distributed in lipids in monomeric form, as proven by Ho, et al. [50].

Based on the quantitative HPLC drug analysis and the fluorescence images, the excellent Hy distribution from LNCs after administration

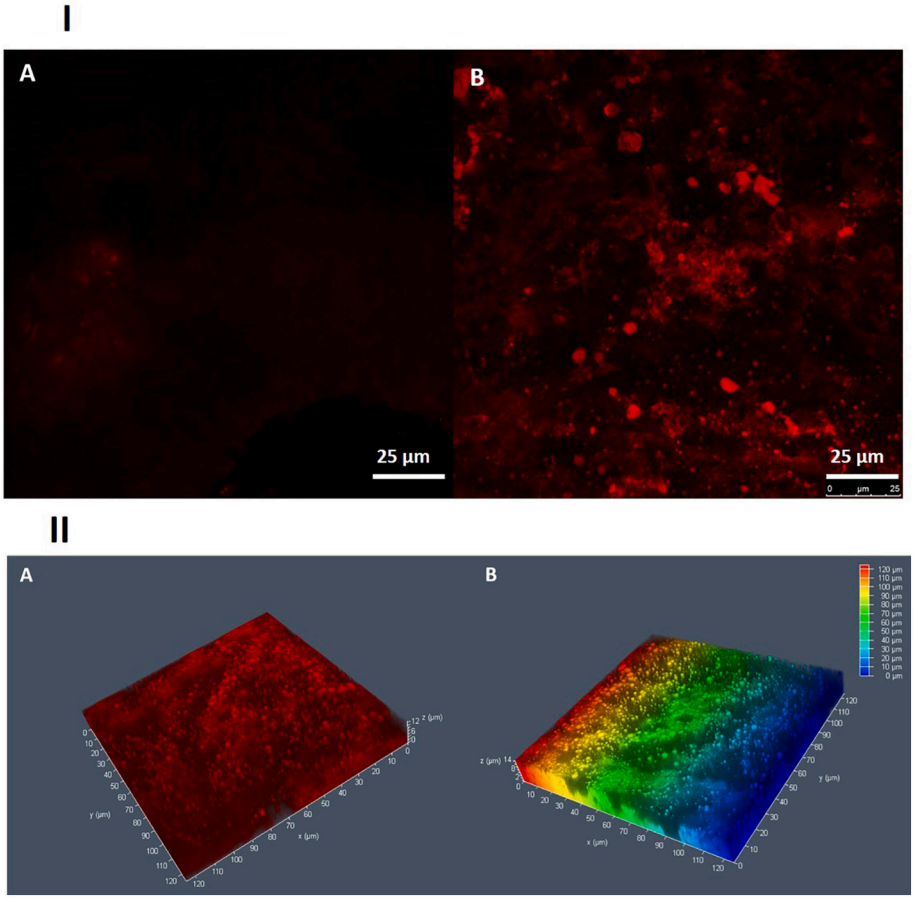

Fig. 8. Confocal fluorescence image of excised full-thickness neonatal porcine skin after injection using AdminPen™ 1200 µm Ho-MNs; **I)** transverse section for **A)** Hy solution as a control, B) Hy-LNCs 2. **II)** Longitudinal 3D *Z*-stack images for **A)** Hy-LNCs 2 and **B)** with depth scaling.

using Ho-MNs could be explained by two main hypotheses. First is the physicochemical nature of the drug. Hy, as a member of the naphtodianthrones family, is known to be poorly soluble in physiological solutions and produces non-fluorescent aggregates [16,21]. These aggregates were found to be stable and remain confined to *SC,* hindering penetration and leading to very poor intradermal distribution [14]. Besides, hydrogen bonding is one of the main factors limiting skin penetration [88]. Hy features six phenolic groups, potentially forming strong hydrogen bonds with the surrounding environment leading to prominent physical interaction with the SC retarding skin penetration and lowering skin recovery [14]. Second, LNCs were proven to maintain stability upon dilution in physiological conditions [54]. Consequently, LNCs succeeded to maintain solubility, photoactivity and distribution of Hy in physiological tissues.

Collectively, *ex vivo* skin deposition study concluded that administration of Hy-LNCs using AdminPen™ Ho-MNs and S-Ho-MN injection significantly improved both the intradermal distribution of Hy within different skin layers and the total cumulative amount of drug deposited in the tissues. This consistent trend would, in turn, improve the therapeutic efficacy of treatment, reduce the frequency of PDT application and improve patient compliance. Moreover, the presented Ho-MN systems combined with LNCs could hypothetically secure the delivery of Hy for enhanced anticancer photodynamic therapeutic outcomes.

In summary, the conducted *in vitro* and *ex vivo* studies confirmed the ability of both types of Ho-MNs in terms of sharpness, length, skin insertion, and effective delivery of Hy-LNCs into the lower layers of the excised neonatal porcine skin.

3.3. Investigation of the overall antitumor efficacy of nanoformulations

To the best of our knowledge, this is the first study to use a combination of LNCs and Ho-MNs to facilitate the intradermal delivery of photosensitisers and to improve the local photodynamic activity. The present study investigates, for the first time, the *in vitro* and *in vivo* antitumour photodynamic efficacy of drug-loaded LNCs after injection with Ho-MNs.

In order to evaluate the *in vivo* photoactivity and anti-tumour efficacy of Hy, female Balb/C nude mice were inoculated with CT-26 (CRL-2638™), a mouse colon cell line, to form subcutaneous tumours. After a few days, plumbs were formed on the dorsal flanks of mice, indicating successful tumour induction. The animals were divided into four groups. The first cohort was kept as the untreated positive control, the second cohort was irradiated with LED light without any drug treatment, the third cohort was treated with Hy-LNCs *via* S-Ho-MN without light irradiation, and the fourth cohort was treated with Hy-LNCs S-Ho-MN and subjected to LED irradiation at 595 ± 10 nm LED light and fluence rate of 45 ± 2 mW cm^{-2}, Fig. 10a. According to Blank, et al., the most pronounced tumour necrosis and vascular damage was caused by Hy after irradiation of mice at 590 nm [12,89].

Mice were carefully examined for weight and normal activity before the administration of each dose. The tumours on the mice were subsequently observed, and the tumour size was measured for each animal after every dose as detailed in Section 2.6.4. The calculated tumour volume (mm^3) was plotted *versus* treatment doses to show the growth profiles in different cohorts of mice. The sufficient number of animals in each group and similarity of tumour volume (100 mm^3) at day 0 facilitated the statistical analysis of obtained data. At the end of the

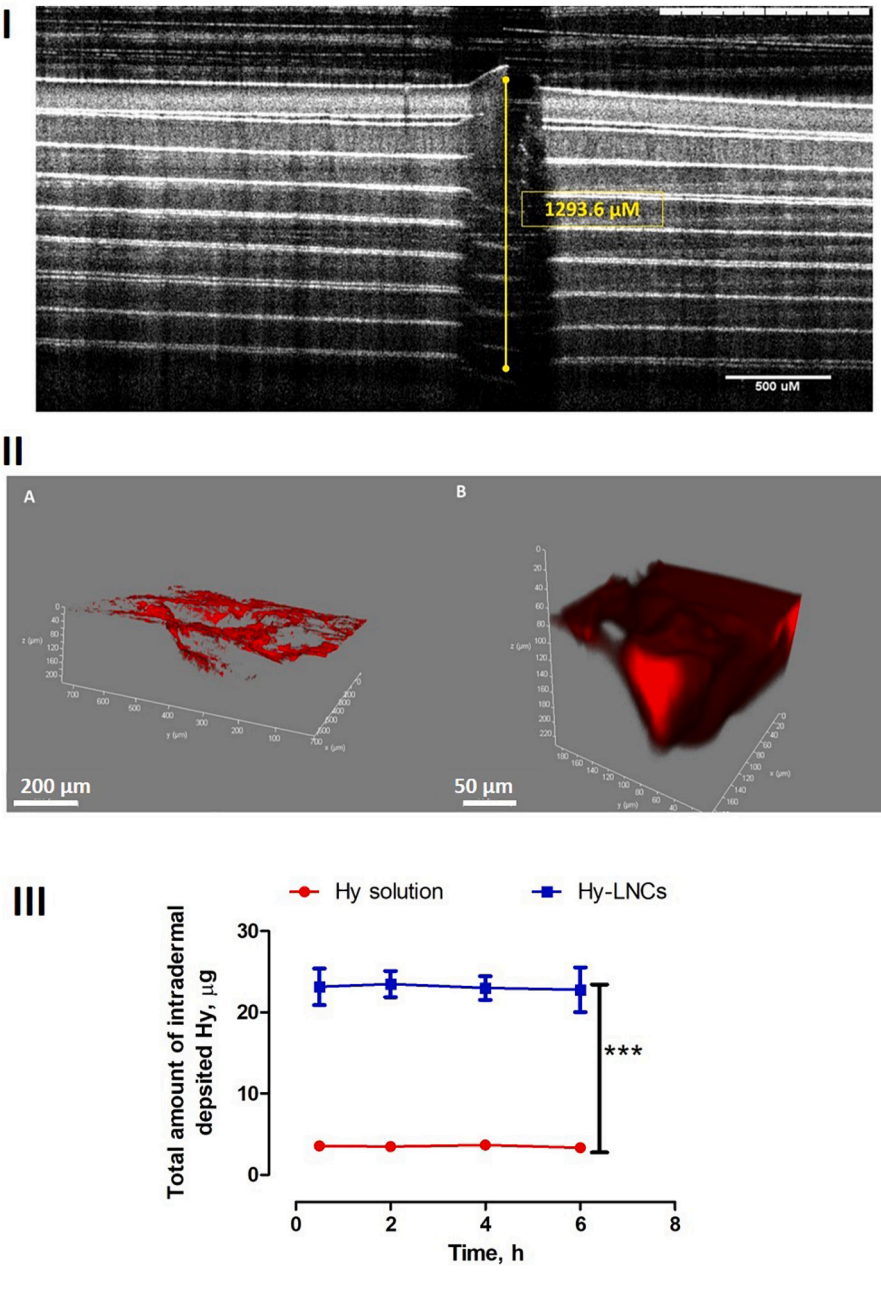

Fig. 9. I) OCT image showing perforated Parafilm M® (≈1.4 mm thickness) as a skin simulant after insertion of S-Ho-MN. **II)** Multiphoton fluorescence 3D Z-stack images of excised neonatal porcine skin 2 h after injection of **A)** Hy solution and **B)** Hy-LNCs 2 using S-Ho-MN. **III)** *Ex vivo* total skin deposition study of Hy solution and Hy-LNCs 2 across excised full-thickness neonatal porcine skin after injection using S-Ho-MN. Injected Hy amount was 25 µg. ***Highly significant difference from Hy control solution (Student's *t*-test, $p < 0.0001$). Data reported as mean ± SD, $n = 3$.

experiment, the mice were humanely sacrificed, and the tumours were harvested and prepared for histological examination.

3.3.1. *Evaluation of Hypericin biodistribution*

Prior to the commencement of antitumour efficacy evaluation, the quality of *in vivo* MNs insertion, formulation delivery and drug biodistribution were examined. An *in vivo* pilot study was performed on healthy Balb/C female nude mice (unpublished data). Hy-LNCs were administered to mice using the AdminPen™ Ho-MNs and fluorescent images were generated using *in vivo* Extreme Bruker. Hy-LNCs were easily monitored in the bodies of the hairless mice due to the inherent fluorescent properties of Hy. The results showed that AdminPen™ Ho-MNs secured successful free-flowing delivery of Hy-LNCs into the skin without any blockage or leakage and the skin retained its barrier properties shortly after administration, Fig. S5. The data also revealed that Hy-LNCs remained confined to the subcutaneous tissue for 1 h before starting to distribute to body organs. Thus, the 45 min, after MNs application, was chosen to be the optimum time to achieve maximum drug retention at the tumour site and thus for the commencement of irradiation.

However, the application of AdminPen™ Ho-MNs to the plumb of tumours in the implanted mice seemed to be tricky, leading to considerable leakage and variations in the applied dose. That could be due to the flat nature of the device that led to imperfect insertion. The fabrication of curved devices with similar properties could be more effective for hyperkeratotic lesions. On the other hand, the inhouse-developed S-Ho-MN showed higher suitability for the delivery of formulations into tumour plumbs without leakage. Therefore, it was the best candidate to proceed with the anti-tumour efficacy study of encapsulated Hy in the animal model.

In addition, the drug biodistribution in tumour-bearing mice was examined prior to irradiation using Bruker image station system. The *in vivo* Bruker fluorescence images showed strong fluorescent signals confirming the localisation of Hy in the tumour site before light

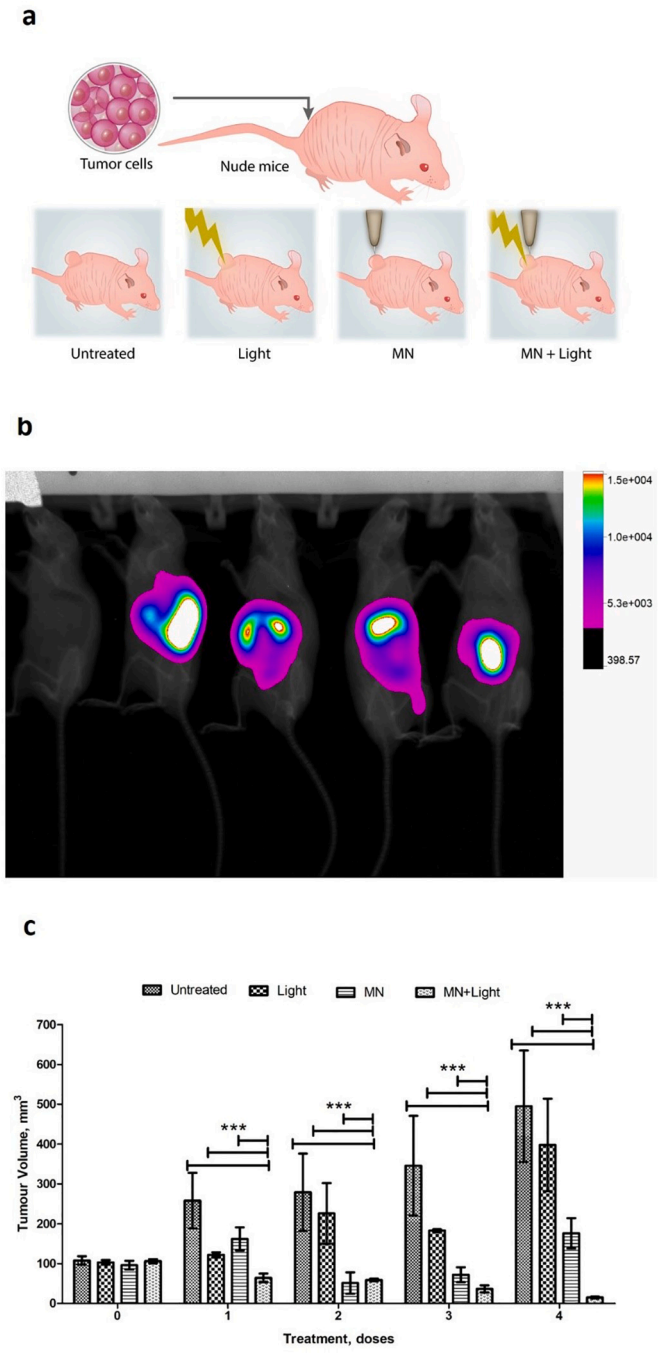

Fig. 10. a) Schematic representation showing the four cohorts investigated in the *in vivo* experiment. **b)** *In vivo* biodistribution imaging using Bruker station system for control (on the left) and MN treated Balb/C female nude mice showing the localisation of Hy after insertion using S-Ho-MN before light application. **c)** Change in tumour volume (mm^3) in four different groups of Balb/C female nude mice. Irradiation was done using a LED of 595 ± 10 nm, I = 450 ± 20 W/m^2. ***Highly significant difference between Hy control solution and untreated mice (One-way ANOVA with Tukey's multiple comparison *post hoc* test, $p < 0.0001$). Data reported as mean ± SD, $n = 4$, at least.

application, Fig. 10b. The administration of Hy *via* Ho-MNs secured a considerably shorter time, 45 min, for maximum drug accumulation at tumour site compared to other delivery routes. For example, the highest Hy accumulation in subcutaneously implanted tumour cell lines in mice was reached 4–6 h post intravenous injection [90]. Similarly, at least 2 h was required after oral administration of Hy to reach its maximum concentration in subcutaneously implanted prostate cancer cells [91].

3.3.2. Evaluation of Hypericin antitumour activity

Considering the tumour growth profile, Fig. 10c, both the control groups (Cohorts 1 and 2) showed a continuous and rapid increase in tumour growth throughout the experiment. Whereas in mice that received Hy-LNCs *via* S-Ho-MN and were exposed to light, the tumour volume significantly reduced from 103 ± 5.16 to 15 ± 2.30 mm^3 with no gross visible mass. It is worth mentioning that, in the absence of light, the effect of S-Ho-MN injected Hy-LNCs was restricted to cause a transient reduction in tumour volume during the experiment, followed by recurrence of tumour growth at a slower rate compared to control animals. Thus, effective tumour destruction (85.84%) was found only when the mice were injected with Hy-LNCs *via* S-Ho-MN and irradiated.

Hy is considered to be a tumour selective agent as it is preferentially up taken to tumour tissue and at the same time eliminated at a slower rate than normal tissues. However, its high hydrophobicity and susceptibility to aggregation in biological systems diminish its biophotoactivity [65,91]. In light of the achieved *in vitro* high singlet oxygen quantum yield, the enhanced intracellular localisation and the deeper dermal distribution, it is not surprising that Hy-LNCs MN delivery system mediated an effective anticancer PDT in animal models upon light activation. Another attractive advantage for the encapsulated photosensitisers is that their *in vivo* photodynamic activity does not rely on the release from their nanocarriers. As reviewed by Tada, and Baptista [92], the photosensitiser could be released from its photosensitizing nanoparticles at the subcellular compartment or it could remain entrapped within the carrier system matrix so the whole system would act as a dual PDT agent with higher therapeutic effect than the dug alone.

In addition, in the current work, MN application of Hy-LNCs achieved the needed drug retention in a short time with a low dose and high efficacy. In an earlier study, 20 mg/Kg of Hy ethanolic solution was administered orally to slow the growth rate of subcutaneous prostate cancer after irradiation, while it was not sufficient to cause tumour destruction [91]. From the same perspective, weekly intratumoural injection of 10 mg/kg tumour of Hy DMSO solution followed by biweekly PDT for over 6–8 weeks *via* surgical laser fibreoptic insertion was required for regression of squamous cell carcinoma (<400 mm^3) in athymic nude mice [12]. Co-encapsulation of Hy (1.25 mg/Kg) and protoporphyrin (1.25 mg/Kg) into LNCs was required to cause a delay in tumour growth without complete eradication after intratumoural injection [22]. Interestingly, the total delivered dose in the present work was only 4 mg/Kg, clearly lower than the previously reported doses administered by other routes.

3.3.3. Histology study

Histological sections of skin samples were prepared using H&E stain and observed with a digital microscope under different magnification powers, Fig. 11. The results revealed that the untreated group showed a dermal and subcutaneous malignant growth formed of diffuse sheets of malignant cells with pleomorphism, hyperchromatism, and brisky mitotic lesions. The light-treated group showed treatment effect in the form of foci of necrosis (red arrow) and fibrosis (blue arrow) with a remarkable amount of residual tumour (yellow arrow). Hy-LNCs-MN treated mice showed treatment effects in the form of extensive necrosis (red arrow) and fibrosis (blue arrow) with a small amount of residual tumour (yellow arrow). Interestingly, mice treated with both light and Hy-LNCs-MN showed an absence of residual tumour and treatment effect in the form of fibrosis (blue arrow). Collectively, histological micrographs confirmed that mice treated with Hy-LNCs *via* S-Ho-MN and subjected to irradiation showed maximum tumour elimination, as deduced by the tumour growth profiles.

To sum up, the route of Hy administration, the designed drug delivery system, the dose of Hy, incubation time with cancer cells, and light irradiation are key limiting factors in the effectiveness of therapy.

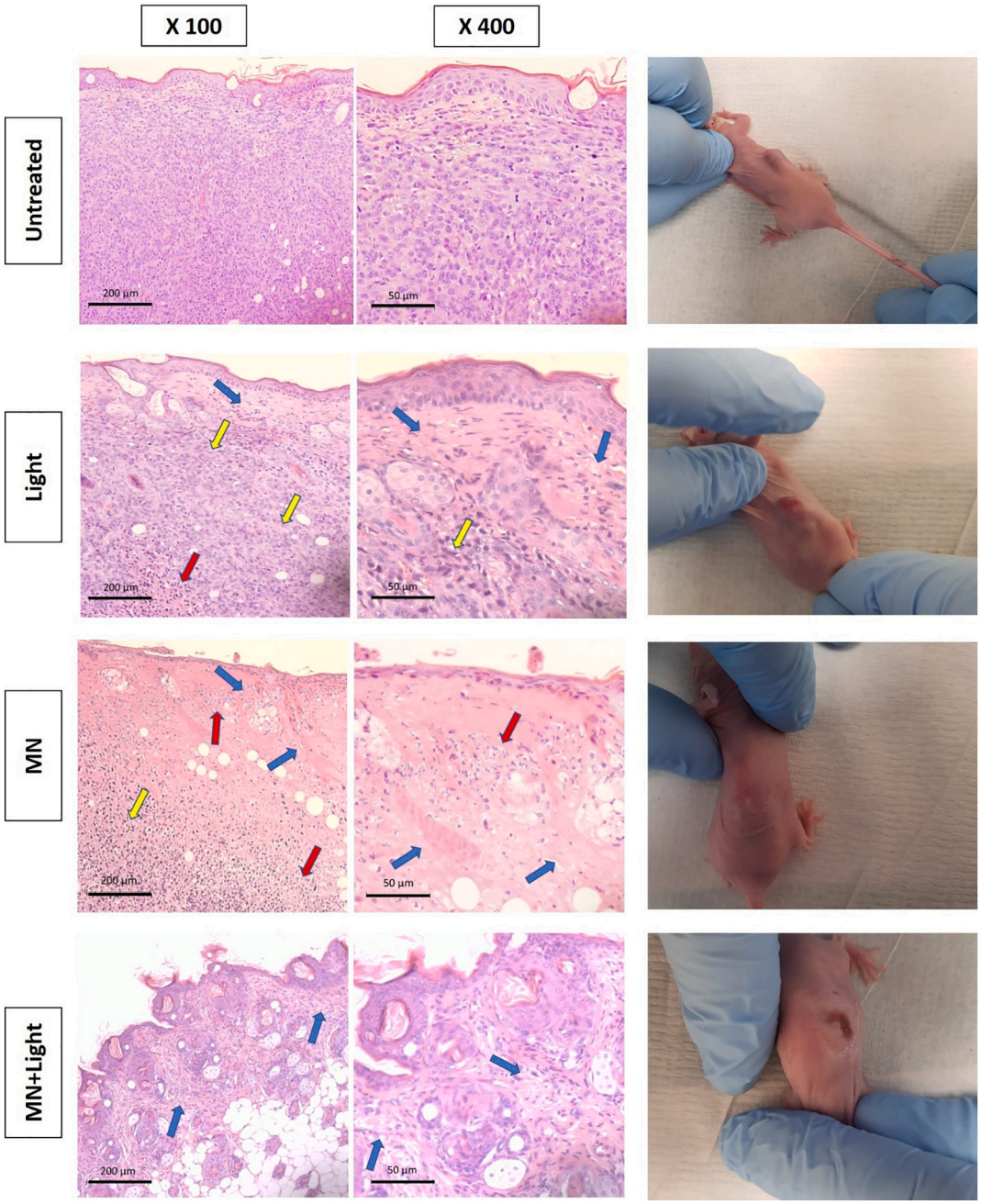

Fig. 11. Microphotographs of histological sections (H&E staining) of untreated, light, MNs and light + MNs treated mice, at magnification powers of x100 and x400, with corresponding tumour growth. Irradiation was done using a LED of 595 ± 10 nm, I = 450 ± 20 W/m^2. Red arrows indicate necrosis, and blue arrows indicate fibrosis, and yellow arrows indicate a residual tumour. (For interpretation of the references to colour in this figure legend, the reader is referred to the web version of this article.)

In the present study, significant tumour ablation was achieved using a lower dose, direct, and minimally invasive treatment strategy without the need for the placement of a laser source inside the tumour for a shorter duration of time.

4. Conclusion

This study unveiled the use of a newly developed Ho-MN device, AdminPen™ Ho-MNs, and an in-house S-Ho-MN integrated with Hy-LNCs as a potential drug delivery platform for local photodynamic cancer therapy, such as non-melanoma skin cancers, based on the following innovative outcomes. First, blank and loaded LNCs were successfully prepared using the phase inversion method with monodisperse particle distribution and high encapsulation efficiency for loaded ones. Second, Hy-LNCs showed enhanced photoactivity, high subcellular localisation, and significant photocytotoxicity. Third, according to the insertion properties testing and the *ex vivo* drug deposition studies, both types of Ho-MNs succeeded in deeply delivering the Hy-LNCs to the viable layer of excised porcine skin. However, S-Ho-MN was superior to AdminPen™ Ho-MNs in terms of ease and feasibility of *in vivo* application to tumour-bearing mice. Finally, animal studies indicated the gross tumour destruction caused by photoactivated Hy-LNCs demonstrating the suitability of S-Ho-MN as a direct delivery system of Hy-LNCs into the tumour site. Remarkably, the presented Hy-LNCs combined Ho-MN delivery strategy successfully tackled the low solubility, susceptible photo-instability and poor biological

photoactivity of Hy, as well as enhanced its *in vivo* photoactive anticancer efficiency. These principal benefits support previously reported data and provide new evidence that Hy-LNCs show promising potential as a local potent photodynamic anticancer agent either alone or as a co-therapeutic modality in combination with chemotherapy, surgery, radiotherapy or immunotherapy. Yet, as a scope for future work, more preclinical and clinical investigations on the safety of Hy-LNCs and the performance of Ho-MNs are required to be conducted.

CRediT authorship contribution statement

Heba Abd-El-Azim: Investigation, Methodology, Formal analysis, Writing – original draft, Writing – review & editing. **Ismaiel A. Tekko:** Investigation, Methodology, Formal analysis, Resources, Writing – review & editing. **Ahlam Ali:** Investigation, Methodology, Resources, Formal analysis. **Alyaa Ramadan:** Investigation, Methodology, Formal analysis, Writing – review & editing. **Noha Nafee:** Investigation, Methodology, Formal analysis, Writing – review & editing. **Nawal Khalafallah:** Investigation, Methodology, Formal analysis, Writing – review & editing. **Taifur Rahman:** Investigation, Methodology, Formal analysis. **William Mcdaid:** Investigation, Methodology, Formal analysis. **Rania G. Aly:** Investigation, Methodology, Formal analysis. **Lalitkumar K. Vora:** Investigation, Methodology, Formal analysis, Writing – review & editing. **Steven J. Bell:** Investigation, Methodology, Resources, Formal analysis. **Fiona Furlong:** Investigation, Methodology, Resources, Formal analysis. **Helen O. McCarthy:** Investigation, Methodology, Resources, Formal analysis. **Ryan F. Donnelly:** Supervision, Investigation, Methodology, Formal analysis, Resources, Funding acquisition, Writing – review & editing.

Acknowledgements

The authors thank the Newton Mosharafa Ph.D. Scholarship Programme that is funded by The Egyptian Ministry of Higher Education and Scientific Research and the British Council for supporting this research.

Appendix A. Supplementary data

Supplementary data to this article can be found online at https://doi.org/10.1016/j.jconrel.2022.06.027.

References

[1] H. Sung, J. Ferlay, R.L. Siegel, M. Laversanne, I. Soerjomataram, A. Jemal, F. Bray, Global Cancer statistics 2020: GLOBOCAN estimates of incidence and mortality worldwide for 36 cancers in 185 countries, CA Cancer J. Clin. 71 (2021) 209–249.

[2] I.M. Ndhundhuma, H. Abrahamse, Susceptibility of in vitro melanoma skin Cancer to Photoactivated Hypericin versus Aluminium(III) Phthalocyanine chloride Tetrasulphonate, Biomed. Res. Int. 2017 (2017), e5407012, https://doi.org/10.1155/2017/5407012.

[3] A.F. dos Santos, D.R.Q. de Almeida, L.F. Terra, M.S. Baptista, L. Labriola, Photodynamic therapy in cancer treatment - an update review, J. Cancer Metastasis Treatment. 5 (2019) 25, https://doi.org/10.20517/2394-4722.2018.83.

[4] N. Dragicevic-Curic, A. Fahr, Liposomes in topical photodynamic therapy, Expert Opin Drug Deliv. 9 (2012) 1015–1032, https://doi.org/10.1517/17425247.2012.697894.

[5] T. Youssef, M. Fadel, R. Fahmy, K. Kassab, Evaluation of hypericin-loaded solid lipid nanoparticles: physicochemical properties, photostability and phototoxicity, Pharm. Dev. Technol. 17 (2012) 177–186, https://doi.org/10.3109/10837450.2010.529148.

[6] C. Bernal, A.O. Ribeiro, G.P. Andrade, J.R. Perussi, Photodynamic efficiency of hypericin compared with chlorin and hematoporphyrin derivatives in HEp-2 and Vero epithelial cell lines, Photodiagn. Photodyn. Ther. 12 (2015) 176–185, https://doi.org/10.1016/j.pdpdt.2015.04.003.

[7] L. Mühleisen, M. Alev, H. Unterweger, D. Subatzus, M. Pöttler, R.P. Friedrich, C. Alexiou, C. Janko, Analysis of Hypericin-mediated effects and implications for targeted photodynamic therapy, Int. J. Mol. Sci. 18 (2017) E1388, https://doi.org/10.3390/ijms18071388.

[8] S. Kwiatkowski, B. Knap, D. Przystupski, J. Saczko, E. Kędzierska, K. Knap-Czop, J. Kotlińska, O. Michel, K. Kotowski, J. Kulbacka, Photodynamic therapy – mechanisms, photosensitizers and combinations, Biomed. Pharmacother. 106 (2018) 1098–1107, https://doi.org/10.1016/j.biopha.2018.07.049.

[9] D. Kacerovská, K. Pizinger, F. Majer, F. Smíd, Photodynamic therapy of nonmelanoma skin cancer with topical *hypericum perforatum* extract–a pilot study, Photochem. Photobiol. 84 (2008) 779–785, https://doi.org/10.1111/j.1751-1097.2007.00260.x.

[10] V.P. Chavda, D. Vihol, B. Mehta, D. Shah, M. Patel, L.K. Vora, M. Pereira-Silva, A. C. Paiva-Santos, Phytochemical-loaded liposomes for anticancer therapy: an updated review, Nanomedicine. 17 (2022) 547–568, https://doi.org/10.2217/nnm-2021-0463.

[11] J. Mikeš, J. Koval, R. Jendželovský, V. Sačková, I. Uhrinová, M. Kello, L. Kuliková, P. Fedoročko, The role of p53 in the efficiency of photodynamic therapy with hypericin and subsequent long-term survival of colon cancer cells, Photochem. Photobiol. Sci. 8 (2009) 1558–1567, https://doi.org/10.1039/B9PP00021F.

[12] C.S. Head, Q. Luu, J. Sercarz, R. Saxton, Photodynamic therapy and tumor imaging of hypericin-treated squamous cell carcinoma, World J Surg Oncol. 4 (2006) 87, https://doi.org/10.1186/1477-7819-4-87.

[13] J. Yi, X. Yang, L. Zheng, G. Yang, L. Sun, Y. Bao, Y. Wu, Y. Huang, C. Yu, S.-N. Yang, Y. Li, Photoactivation of hypericin decreases the viability of RINm5F insulinoma cells through reduction in JNK/ERK phosphorylation and elevation of caspase-9/caspase-3 cleavage and Bax-to-Bcl-2 ratio, Biosci. Rep. 35 (2015), e00195, https://doi.org/10.1042/BSR20150028.

[14] A. Boiy, R. Roelandts, T. Roskams, P.A.M. de Witte, Effect of vehicles and esterification on the penetration and distribution of hypericin in the skin of hairless mice, Photodiagn. Photodyn. Ther. 4 (2007) 130–139, https://doi.org/10.1016/j.pdpdt.2007.02.002.

[15] H. Unterweger, D. Subatzus, R. Tietze, C. Janko, M. Poettler, A. Stiegelschmitt, M. Schuster, C. Maake, A.R. Boccaccini, C. Alexiou, Hypericin-bearing magnetic iron oxide nanoparticles for selective drug delivery in photodynamic therapy, IJN. 10 (2015) 6985–6996, https://doi.org/10.2147/IJN.S92336.

[16] M. Zeisser-Labouèbe, N. Lange, R. Gurny, F. Delie, Hypericin-loaded nanoparticles for the photodynamic treatment of ovarian cancer, Int. J. Pharm. 326 (2006) 174–181, https://doi.org/10.1016/j.ijpharm.2006.07.012.

[17] N. Nafee, A. Youssef, H. El-Gowelli, H. Asem, S. Kandil, Antibiotic-free nanotherapeutics: Hypericin nanoparticles thereof for improved in vitro and in vivo antimicrobial photodynamic therapy and wound healing, Int. J. Pharm. 454 (2013) 249–258, https://doi.org/10.1016/j.ijpharm.2013.06.067.

[18] A.M. Lima, C.D. Pizzol, F.B.F. Monteiro, T.B. Creczynski-Pasa, G.P. Andrade, A. O. Ribeiro, J.R. Perussi, Hypericin encapsulated in solid lipid nanoparticles: phototoxicity and photodynamic efficiency, J. Photochem. Photobiol. B 125 (2013) 146–154, https://doi.org/10.1016/j.jphotobiol.2013.05.010.

[19] A. Pucek, B. Tokarek, E. Waglewska, U. Bazylińska, Recent advances in the structural Design of Photosensitive Agent Formulations Using "soft" colloidal Nanocarriers, Pharmaceutics. 12 (2020) E587, https://doi.org/10.3390/pharmaceutics12060587.

[20] K. Patel, S. Padhye, M. Nagarsenker, Duloxetine HCl lipid nanoparticles: preparation, characterization, and dosage form design, AAPS PharmSciTech 13 (2012) 125–133, https://doi.org/10.1208/s12249-011-9727-6.

[21] A. Barras, L. Boussekey, E. Courtade, R. Boukherroub, Hypericin-loaded lipid nanocapsules for photodynamic cancer therapy in vitro, Nanoscale. 5 (2013) 10562–10572, https://doi.org/10.1039/C3NR02724D.

[22] A. Barras, N. Skandrani, M.G. Pisfil, S. Paryzhak, T. Dumych, A. Haustrate, L. Héliot, T. Gharbi, H. Boulahdour, V. Lehen'kyi, R. Bilyy, S. Szunerits, G. Bidaux, R. Boukherroub, Improved photodynamic effect through encapsulation of two photosensitizers in lipid nanocapsules, J. Mater. Chem. B 6 (2018) 5949–5963, https://doi.org/10.1039/C8TB01759J.

[23] M.M.A. Abdel-Mottaleb, D. Neumann, A. Lamprecht, Lipid nanocapsules for dermal application: a comparative study of lipid-based versus polymer-based nanocarriers, Eur. J. Pharm. Biopharm. 79 (2011) 36–42, https://doi.org/10.1016/j.ejpb.2011.04.009.

[24] H. Zhou, Y. Yue, G. Liu, Y. Li, J. Zhang, Z. Yan, M. Duan, Characterisation and skin distribution of lecithin-based coenzyme Q10-loaded lipid Nanocapsules, Nanoscale Res. Lett. 5 (2010) 1561–1569, https://doi.org/10.1007/s11671-010-9677-z.

[25] L.K. Vora, K. Moffatt, I.A. Tekko, A.J. Paredes, F. Volpe-Zanutto, D. Mishra, K. Peng, R. Raj Singh Thakur, R.F. Donnelly, Microneedle array systems for long-acting drug delivery, Eur. J. Pharm. Biopharm. 159 (2021) 44–76, https://doi.org/10.1016/j.ejpb.2020.12.006.

[26] A.J. Paredes, F. Volpe-Zanutto, A.D. Permana, A.J. Murphy, C.J. Picco, L.K. Vora, J. A. Coulter, R.F. Donnelly, Novel tip-loaded dissolving and implantable microneedle array patches for sustained release of finasteride, Int. J. Pharm. 606 (2021), 120885, https://doi.org/10.1016/j.ijpharm.2021.120885.

[27] A.J. Paredes, I.K. Ramöller, P.E. McKenna, M.T.A. Abbate, F. Volpe-Zanutto, L. K. Vora, M. Kilbourne-Brook, C. Jarrahian, K. Moffatt, C. Zhang, I.A. Tekko, R. F. Donnelly, Microarray patches: breaking down the barriers to contraceptive care and HIV prevention for women across the globe, Adv. Drug Deliv. Rev. 173 (2021) 331–348, https://doi.org/10.1016/j.addr.2021.04.002.

[28] I.A. Tekko, L.K. Vora, F. Volpe-Zanutto, K. Moffatt, C. Jarrahian, H.O. McCarthy, R. F. Donnelly, Novel bilayer microarray patch-assisted long-acting Micro-depot Cabotegravir intradermal delivery for HIV pre-exposure prophylaxis, Adv. Funct. Mater. 32 (2022) 2106999, https://doi.org/10.1002/adfm.202106999.

[29] L.K. Vora, A.J. Courtenay, I.A. Tekko, E. Larrañeta, R.F. Donnelly, Pullulan-based dissolving microneedle arrays for enhanced transdermal delivery of small and large biomolecules, Int. J. Biol. Macromol. 146 (2020) 290–298, https://doi.org/10.1016/j.ijbiomac.2019.12.184.

[30] Á. Cárcamo-Martínez, B. Mallon, J. Domínguez-Robles, L.K. Vora, Q.K. Anjani, R. F. Donnelly, Hollow microneedles: a perspective in biomedical applications, Int. J. Pharm. 599 (2021), 120455, https://doi.org/10.1016/j.ijpharm.2021.120455.
[31] E. Larrañeta, L. Vora, Delivery of Nanomedicines Using Microneedles, Wiley Online Library, 2018, pp. 177–205, https://doi.org/10.1002/9781119305101.ch6, accessed April 19, 2022.
[32] J.D. Clogston, A.K. Patri, Zeta potential measurement, Methods Mol. Biol. 697 (2011) 63–70, https://doi.org/10.1007/978-1-60327-198-1_6.
[33] K. Patel, M. Tyagi, J. Monpara, L. Vora, S. Gupta, P. Vavia, Arginoplexes: an arginine-anchored nanoliposomal carrier for gene delivery, J. Nanopart. Res. 16 (2014) 2345, https://doi.org/10.1007/s11051-014-2345-y.
[34] M.I. Nasiri, L.K. Vora, J.A. Ershaid, K. Peng, I.A. Tekko, R.F. Donnelly, Nanoemulsion-based dissolving microneedle arrays for enhanced intradermal and transdermal delivery, Drug Deliv. and Transl. Res. 12 (2022) 881–896, https://doi.org/10.1007/s13346-021-01107-0.
[35] L. Vora, M. Tyagi, K. Patel, S. Gupta, P. Vavia, Self-assembled nanocomplexes of anionic pullulan and polyallylamine for DNA and pH-sensitive intracellular drug delivery, J. Nanopart. Res. 16 (2014) 2781, https://doi.org/10.1007/s11051-014-2781-8.
[36] F.B. Borghi-Pangoni, M.V. Junqueira, S.B. de Souza Ferreira, L.L. Silva, B. R. Rabello, L.V. de Castro, M.L. Baesso, A. Diniz, W. Caetano, M.L. Bruschi, Preparation and characterization of bioadhesive system containing hypericin for local photodynamic therapy, Photodiagn. Photodyn. Ther. 19 (2017) 284–297, https://doi.org/10.1016/j.pdpdt.2017.06.016.
[37] F. Piccinini, A. Tesei, C. Arienti, A. Bevilacqua, Cell counting and viability assessment of 2D and 3D cell cultures: expected reliability of the trypan blue assay, Biol. Proced. Online. 19 (2017) 8, https://doi.org/10.1186/s12575-017-0056-3.
[38] K. Peng, L.K. Vora, I.A. Tekko, A.D. Permana, J. Domínguez-Robles, D. Ramadon, P. Chambers, H.O. McCarthy, E. Larrañeta, R.F. Donnelly, Dissolving microneedle patches loaded with amphotericin B microparticles for localised and sustained intradermal delivery: potential for enhanced treatment of cutaneous fungal infections, J. Control. Release 339 (2021) 361–380, https://doi.org/10.1016/j.jconrel.2021.10.001.
[39] M. Mir, A.D. Permana, I.A. Tekko, H.O. McCarthy, N. Ahmed, Asim Ur Rehman, R. F. Donnelly, Microneedle liquid injection system assisted delivery of infection responsive nanoparticles: a promising approach for enhanced site-specific delivery of carvacrol against polymicrobial biofilms-infected wounds, Int. J. Pharm. 587 (2020), 119643, https://doi.org/10.1016/j.ijpharm.2020.119643.
[40] E. Altuntaş, I.A. Tekko, L.K. Vora, N. Kumar, R. Brodsky, O. Chevallier, E. McAlister, Q. Kurnia Anjani, H.O. McCarthy, R.F. Donnelly, Nestorone nanosuspension-loaded dissolving microneedles array patch: a promising novel approach for "on-demand" hormonal female-controlled peritcoital contraception, Int. J. Pharm. 614 (2022), 121422, https://doi.org/10.1016/j.ijpharm.2021.121422.
[41] A.D. Permana, M.T.C. McCrudden, R.F. Donnelly, Enhanced intradermal delivery of Nanosuspensions of Antifilariasis drugs using dissolving microneedles: a proof of concept study, Pharmaceutics. 11 (2019) E346, https://doi.org/10.3390/pharmaceutics11070346.
[42] Y. Wu, L.K. Vora, D. Mishra, M.F. Adrianto, S. Gade, A.J. Paredes, R.F. Donnelly, T. R.R. Singh, Nanosuspension-loaded dissolving bilayer microneedles for hydrophobic drug delivery to the posterior segment of the eye, biomaterials, Advances. (2022), 212767, https://doi.org/10.1016/j.bioadv.2022.212767.
[43] M. Mir, N. Ahmed, A.D. Permana, A.M. Rodgers, R.F. Donnelly, A.U. Rehman, Enhancement in site-specific delivery of Carvacrol against methicillin resistant Staphylococcus aureus induced skin infections using enzyme responsive nanoparticles: a proof of concept study, Pharmaceutics. 11 (2019) E606, https://doi.org/10.3390/pharmaceutics11110606.
[44] A.A. Albadr, I.A. Tekko, L.K. Vora, A.A. Ali, G. Laverty, R.F. Donnelly, R.R. S. Thakur, Rapidly dissolving microneedle patch of amphotericin B for intracorneal fungal infections, Drug Deliv. and Transl. Res. 12 (2022) 931–943, https://doi.org/10.1007/s13346-021-01032-2.
[45] X. Wang, J. Mi, Y. Dong, J. Yang, Optimization of Extraction Process of Hypericin from St. John's Wort by Central Composite Design-Response Surface Methodology 9, 2014.
[46] A. Faustino-Rocha, P.A. Oliveira, J. Pinho-Oliveira, C. Teixeira-Guedes, R. Soares-Maia, R.G. da Costa, B. Colaço, M.J. Pires, J. Colaço, R. Ferreira, M. Ginja, Estimation of rat mammary tumor volume using caliper and ultrasonography measurements, Lab Anim (NY). 42 (2013) 217–224, https://doi.org/10.1038/laban.254.
[47] B. Heurtault, P. Saulnier, B. Pech, J.-E. Proust, J.-P. Benoit, A novel phase inversion-based process for the preparation of lipid nanocarriers, Pharm. Res. 19 (2002) 875–880, https://doi.org/10.1023/a:1016121319668.
[48] A. Vonarbourg, P. Saulnier, C. Passirani, J.-P. Benoit, Electrokinetic properties of noncharged lipid nanocapsules: influence of the dipolar distribution at the interface, Electrophoresis. 26 (2005) 2066–2075, https://doi.org/10.1002/elps.200410145.
[49] D. Puro, R. Athawale, A. Pandya, Design, optimization and characterization of nanostructured lipid carriers of Raloxifene hydrochloride for transdermal delivery, Nanosci. Nanotechnol. Asia. 10 (2021) 57–67.
[50] Y.-F. Ho, M.-H. Wu, B.-H. Cheng, Y.-W. Chen, M.-C. Shih, Lipid-mediated preferential localization of hypericin in lipid membranes, Biochim. Biophys. Acta 1788 (2009) 1287–1295, https://doi.org/10.1016/j.bbamem.2009.01.017.
[51] A. Lamprecht, Y. Bouligand, J.-P. Benoit, New lipid nanocapsules exhibit sustained release properties for amiodarone, J. Control. Release 84 (2002) 59–68, https://doi.org/10.1016/s0168-3659(02)00258-4.
[52] A. Barras, A. Mezzetti, A. Richard, S. Lazzaroni, S. Roux, P. Melnyk, D. Betbeder, N. Monfilliette-Dupont, Formulation and characterization of polyphenol-loaded lipid nanocapsules, Int. J. Pharm. 379 (2009) 270–277, https://doi.org/10.1016/j.ijpharm.2009.05.054.
[53] A.C. Groo, M. Bossiere, L. Trichard, P. Legras, J.P. Benoit, F. Lagarce, In vivo evaluation of paclitaxel-loaded lipid nanocapsules after intravenous and oral administration on resistant tumor, Nanomedicine (London) 10 (2015) 589–601, https://doi.org/10.2217/nnm.14.124.
[54] G. Lollo, G.R. Rivera-Rodriguez, J. Bejaud, T. Montier, C. Passirani, J.-P. Benoit, M. García-Fuentes, M.J. Alonso, D. Torres, Polyglutamic acid-PEG nanocapsules as long circulating carriers for the delivery of docetaxel, Eur. J. Pharm. Biopharm. 87 (2014) 47–54, https://doi.org/10.1016/j.ejpb.2014.02.004.
[55] F. Fischer, G. Graschew, H.-J. Sinn, W. Maier-Borst, W.J. Lorenz, P.M. Schlag, A chemical dosimeter for the determination of the photodynamic activity of photosensitizers, Clin. Chim. Acta 274 (1998) 89–104, https://doi.org/10.1016/S0009-8981(98)00045-X.
[56] Y.N. Konan, R. Gurny, E. Allémann, State of the art in the delivery of photosensitizers for photodynamic therapy, J. Photochem. Photobiol. B Biol. 66 (2002) 89–106, https://doi.org/10.1016/S1011-1344(01)00267-6.
[57] B.M. Estevão, D.S. Pellosi, C.F. de Freitas, D. Vanzin, D.S. Franciscato, W. Caetano, N. Hioka, Interaction of eosin and its ester derivatives with aqueous biomimetic micelles: evaluation of photodynamic potentialities, J. Photochem. Photobiol. A Chem. 287 (2014) 30–39, https://doi.org/10.1016/j.jphotochem.2014.04.015.
[58] L.M. Rossi, P.R. Silva, L.L.R. Vono, A.U. Fernandes, D.B. Tada, M.S. Baptista, Protoporphyrin IX nanoparticle carrier: preparation, optical properties, and singlet oxygen generation, Langmuir. 24 (2008) 12534–12538, https://doi.org/10.1021/la800840k.
[59] E. Gianotti, B.M. Estevão, I. Miletto, S. Tonello, F. Renò, L. Marchese, Verteporfin based silica nanoplatform for photodynamic therapy, ChemistrySelect. 1 (2016) 127–131.
[60] X. Li, S. Lee, J. Yoon, Supramolecular photosensitizers rejuvenate photodynamic therapy, Chem. Soc. Rev. 47 (2018) 1174–1188, https://doi.org/10.1039/C7CS00594F.
[61] D. Bechet, P. Couleaud, C. Frochot, M.-L. Viriot, F. Guillemin, M. Barberi-Heyob, Nanoparticles as vehicles for delivery of photodynamic therapy agents, Trends Biotechnol. 26 (2008) 612–621, https://doi.org/10.1016/j.tibtech.2008.07.007.
[62] J. Nel, F. Franconi, N. Joudiou, P. Saulnier, B. Gallez, L. Lemaire, Lipid nanocapsules as in vivo oxygen sensors using magnetic resonance imaging, Mater. Sci. Eng. C 101 (2019) 396–403, https://doi.org/10.1016/j.msec.2019.03.104.
[63] L. Mazzarino, C. Dora, I. Bellettini, E. Minatti, S. Cardoso, E. Senna, Curcumin-loaded polymeric and lipid nanocapsules: preparation, characterization and chemical stability evaluation, Lat. Am. J. Pharm. 29 (2010) 933–940.
[64] U. Bazylińska, A. Lewińska, Ł. Lamch, K.A. Wilk, Polymeric nanocapsules and nanospheres for encapsulation and long sustained release of hydrophobic cyanine-type photosensitizer, Colloids Surf. A Physicochem. Eng. Asp. 442 (2014) 42–49, https://doi.org/10.1016/j.colsurfa.2013.02.023.
[65] K.M. Davids, The anticancer activity of Hypericin in photodynamic therapy, JBABM. s6 (2012), https://doi.org/10.4172/1948-593X.S6-004.
[66] M. Szwed, M.L. Torgersen, R.V. Kumari, S.K. Yadava, S. Pust, T.G. Iversen, T. Skotland, J. Giri, K. Sandvig, Biological response and cytotoxicity induced by lipid nanocapsules, J. Nanobiotechnol. 18 (2020) 5, https://doi.org/10.1186/s12951-019-0567-y.
[67] A. Paillard, F. Hindré, C. Vignes-Colombeix, J.-P. Benoit, E. Garcion, The importance of endo-lysosomal escape with lipid nanocapsules for drug subcellular bioavailability, Biomaterials. 31 (2010) 7542–7554, https://doi.org/10.1016/j.biomaterials.2010.06.024.
[68] A. Karioti, A.R. Bilia, Hypericins as potential leads for new therapeutics, Int. J. Mol. Sci. 11 (2010) 562–594, https://doi.org/10.3390/ijms11020562.
[69] C. Maupas, B. Moulari, A. Béduneau, A. Lamprecht, Y. Pellequer, Surfactant dependent toxicity of lipid nanocapsules in HaCaT cells, Int. J. Pharm. 411 (2011) 136–141, https://doi.org/10.1016/j.ijpharm.2011.03.056.
[70] E. McAlister, M. Kirkby, J. Domínguez-Robles, A.J. Paredes, Q.K. Anjani, K. Moffatt, L.K. Vora, A.R. Hutton, P.E. McKenna, E. Larrañeta, The role of microneedle arrays in drug delivery and patient monitoring to prevent diabetes induced fibrosis, Adv. Drug Deliv. Rev. 175 (2021), 113825.
[71] F. Volpe-Zanutto, L.T. Ferreira, A.D. Permana, M. Kirkby, A.J. Paredes, L.K. Vora, A.P. Bonfanti, I. Charlie-Silva, C. Raposo, M.C. Figueiredo, I.M.O. Sousa, A. Brisibe, F.T.M. Costa, R.F. Donnelly, M.A. Foglio, Artemether and lumefantrine dissolving microneedle patches with improved pharmacokinetic performance and antimalarial efficacy in mice infected with plasmodium yoelii, J. Control. Release 333 (2021) 298–315, https://doi.org/10.1016/j.jconrel.2021.03.036.
[72] I.A. Tekko, A.D. Permana, L. Vora, T. Hatahet, H.O. McCarthy, R.F. Donnelly, Localised and sustained intradermal delivery of methotrexate using nanocrystal-loaded microneedle arrays: potential for enhanced treatment of psoriasis, Eur. J. Pharm. Sci. 152 (2020), 105469.
[73] L.K. Vora, R.F. Donnelly, E. Larrañeta, P. González-Vázquez, R.R.S. Thakur, P. R. Vavia, Novel bilayer dissolving microneedle arrays with concentrated PLGA nano-microparticles for targeted intradermal delivery: proof of concept, J. Control. Release 265 (2017) 93–101, https://doi.org/10.1016/j.jconrel.2017.10.005.
[74] S. Rojekar, L.K. Vora, I.A. Tekko, F. Volpe-Zanutto, H.O. McCarthy, P.R. Vavia, R. F. Donnelly, Etravirine-loaded dissolving microneedle arrays for long-acting delivery, Eur. J. Pharm. Biopharm. 165 (2021) 41–51, https://doi.org/10.1016/j.ejpb.2021.04.024.
[75] Á. Cárcamo-Martínez, B. Mallon, Q.K. Anjani, J. Domínguez-Robles, E. Utomo, L. K. Vora, I.A. Tekko, E. Larrañeta, R.F. Donnelly, Enhancing intradermal delivery of tofacitinib citrate: comparison between powder-loaded hollow microneedle arrays

and dissolving microneedle arrays, Int. J. Pharm. 593 (2021), 120152, https://doi.org/10.1016/j.ijpharm.2020.120152.
[76] K. Ita, Transdermal delivery of drugs with microneedles—potential and challenges, Pharmaceutics. 7 (2015) 90–105, https://doi.org/10.3390/pharmaceutics7030090.
[77] V.V. Yuzhakov, Microneedle Array, Patch, and Applicator for Transdermal Drug Delivery, WO2007081430A3. https://patents.google.com/patent/WO2007081430A3/en, 2008.
[78] S.A. Tawde, L. Chablani, A. Akalkotkar, M.J. D'Souza, Evaluation of microparticulate ovarian cancer vaccine via transdermal route of delivery, J. Control. Release 235 (2016) 147–154, https://doi.org/10.1016/j.jconrel.2016.05.058.
[79] A. Juluri, N. Modepalli, S. Jo, M.A. Repka, H.N. Shivakumar, S.N. Murthy, Minimally invasive transdermal delivery of iron-dextran, J. Pharm. Sci. 102 (2013) 987–993, https://doi.org/10.1002/jps.23429.
[80] H.X. Nguyen, A.K. Banga, Enhanced skin delivery of vismodegib by microneedle treatment, Drug Deliv. and Transl. Res. 5 (2015) 407–423, https://doi.org/10.1007/s13346-015-0241-3.
[81] K.N.J. Burger, R.W.H.M. Staffhorst, H.C. de Vijlder, M.J. Velinova, P.H. Bomans, P. M. Frederik, B. de Kruijff, Nanocapsules: lipid-coated aggregates of cisplatin with high cytotoxicity, Nat. Med. 8 (2002) 81–84, https://doi.org/10.1038/nm0102-81.
[82] F.J. Verbaan, S.M. Bal, D.J. van den Berg, J.A. Dijksman, M. van Hecke, H. Verpoorten, A. van den Berg, R. Luttge, J.A. Bouwstra, Improved piercing of microneedle arrays in dermatomed human skin by an impact insertion method, J. Control. Release 128 (2008) 80–88, https://doi.org/10.1016/j.jconrel.2008.02.009.
[83] F.J. Verbaan, S.M. Bal, D.J. van den Berg, W.H.H. Groenink, H. Verpoorten, R. Lüttge, J.A. Bouwstra, Assembled microneedle arrays enhance the transport of compounds varying over a large range of molecular weight across human dermatomed skin, J. Control. Release 117 (2007) 238–245, https://doi.org/10.1016/j.jconrel.2006.11.009.
[84] A.S. Cordeiro, I.A. Tekko, M.H. Jomaa, L. Vora, E. McAlister, F. Volpe-Zanutto, M. Nethery, P.T. Baine, N. Mitchell, D.W. McNeill, R.F. Donnelly, Two-photon polymerisation 3D printing of microneedle Array templates with versatile designs: application in the development of polymeric drug delivery systems, Pharm. Res. 37 (2020) 174, https://doi.org/10.1007/s11095-020-02887-9.
[85] R. Kong, R. Bhargava, Characterization of porcine skin as a model for human skin studies using infrared spectroscopic imaging, Analyst. 136 (2011) 2359–2366, https://doi.org/10.1039/c1an15111h.
[86] E. Larrañeta, J. Moore, E.M. Vicente-Pérez, P. González-Vázquez, R. Lutton, A. D. Woolfson, R.F. Donnelly, A proposed model membrane and test method for microneedle insertion studies, Int. J. Pharm. 472 (2014) 65–73, https://doi.org/10.1016/j.ijpharm.2014.05.042.
[87] L. Wei-Ze, H. Mei-Rong, Z. Jian-Ping, Z. Yong-Qiang, H. Bao-Hua, L. Ting, Z. Yong, Super-short solid silicon microneedles for transdermal drug delivery applications, Int. J. Pharm. 389 (2010) 122–129, https://doi.org/10.1016/j.ijpharm.2010.01.024.
[88] W.J. Pugh, M.S. Roberts, J. Hadgraft, Epidermal permeability — penetrant structure relationships: 3. The effect of hydrogen bonding interactions and molecular size on diffusion across the stratum corneum, Int. J. Pharm. 138 (1996) 149–165, https://doi.org/10.1016/0378-5173(96)04533-4.
[89] M. Blank, G. Kostenich, G. Lavie, S. Kimel, Y. Keisari, A. Orenstein, Wavelength-dependent properties of photodynamic therapy using hypericin in vitro and in an animal model, Photochem. Photobiol. 76 (2002) 335–340, https://doi.org/10.1562/0031-8655(2002)076<0335:wdpopt>2.0.co;2.
[90] H.-Y. Du, B.-H. Bay, M. Olivo, Biodistribution and photodynamic therapy with hypericin in a human NPC murine tumor model, Int. J. Oncol. 22 (2003) 1019–1024.
[91] X. Xie, J.B. Hudson, E.S. Guns, Tumor-specific and photodependent cytotoxicity of hypericin in the human LNCaP prostate tumor model, Photochem. Photobiol. 74 (2001) 221–225, https://doi.org/10.1562/0031-8655(2001)074<0221:tsapco>2.0.co;2.
[92] D.B. Tada, M.S. Baptista, Photosensitizing nanoparticles and the modulation of ROS generation, Front. Chem. 3 (2015), https://doi.org/10.3389/fchem.2015.00033.